ARTICLES
https://doi.org/10.1038/s41564-022-01119-7
nature microbiology

Check for updates

An orally available M^{pro} inhibitor is effective against wild-type SARS-CoV-2 and variants including Omicron

Bao-Xue Quan[1,6], Huiping Shuai[2,6], An-Jie Xia[1,6], Yuxin Hou[2,6], Rui Zeng[1,3,6], Xin-Lei Liu[1,6], Gui-Feng Lin[1,6], Jing-Xin Qiao[1,6], Wen-Pei Li[1], Fa-Lu Wang[1], Kai Wang[1,3], Ren-Jie Zhou[1,3], Terrence Tsz-Tai Yuen[2], Ming-Xin Chen[1], Chaemin Yoon[2], Ming Wu[1], Shi-Yu Zhang[1], Chong Huang[1], Yi-Fei Wang[1], Wei Yang[1], Chenyu Tian[1], Wei-Min Li[1], Yu-Quan Wei[1], Kwok-Yung Yuen[2,4,5], Jasper Fuk-Woo Chan[2,4,5]✉, Jian Lei[1,3]✉, Hin Chu[2]✉ and Shengyong Yang[1]✉

Emerging SARS-CoV-2 variants continue to cause waves of new infections globally. Developing effective antivirals against SARS-CoV-2 and its variants is an urgent task. The main protease (M^{pro}) of SARS-CoV-2 is an attractive drug target because of its central role in viral replication and its conservation among variants. We herein report a series of potent α-ketoamide-containing M^{pro} inhibitors obtained using the Ugi four-component reaction. The prioritized compound, Y180, showed an IC$_{50}$ of 8.1 nM against SARS-CoV-2 M^{pro} and had oral bioavailability of 92.9%, 31.9% and 85.7% in mice, rats and dogs, respectively. Y180 protected against wild-type SARS-CoV-2, B.1.1.7 (Alpha), B.1.617.1 (Kappa) and P.3 (Theta), with EC$_{50}$ of 11.4, 20.3, 34.4 and 23.7 nM, respectively. Oral treatment with Y180 displayed a remarkable antiviral potency and substantially ameliorated the virus-induced tissue damage in both nasal turbinate and lung of B.1.1.7-infected K18-human ACE2 (K18-hACE2) transgenic mice. Therapeutic treatment with Y180 improved the survival of mice from 0 to 44.4% ($P = 0.0086$) upon B.1.617.1 infection in the lethal infection model. Importantly, Y180 was also highly effective against the B.1.1.529 (Omicron) variant both in vitro and in vivo. Overall, our study provides a promising lead compound for oral drug development against SARS-CoV-2.

The coronavirus disease 2019 (COVID-19) pandemic caused by severe acute respiratory syndrome coronavirus 2 (SARS-CoV-2) has affected nearly 290 million patients with more than 5 million deaths as of late December 2021 (https://covid19.who.int/). Despite great success in vaccines, unexpected mutations of the SARS-CoV-2 virus genome bring substantial challenges to the effectiveness of current vaccines[1]. Particularly, the Omicron[2] variant has been demonstrated to be able to escape the protection of current vaccines[3]. Moreover, the likelihood of SARS-CoV-2 to exist for a long time[4] highlights the critical importance of safe and effective antivirals. Unfortunately, treatment options for COVID-19 remain limited[5]. Considering the current situation of the pandemic and possible future needs, drug discovery for SARS-CoV-2 must be expedited as much as possible.

The main protease (M^{pro}, also named 3CL protease) of SARS-CoV-2 plays a key role in the viral life cycle and is conserved among various variants of concern (Supplementary Fig. 1)[6–8]. Thus, M^{pro} is a promising target for antiviral drug development. Currently, a number of SARS-CoV-2 M^{pro} inhibitors have been reported[9–21]. The majority of them belong to peptidomimetics, which are often linked to poor pharmacokinetic (PK) properties. Recently, several research efforts have been made to improve the PK properties of peptidomimetic M^{pro} inhibitors[9–18], but limited progress has been achieved for optimal oral bioavailability[13,17], with only one orally administrated compound (PF-07321332) just being approved for clinical use by the US Food and Drug Administration (FDA)[17], and one (S-217622) still in late clinical trials[19]. Orally available antivirals are highly desirable as patients can be treated as outpatients without overburdening the healthcare system. We herein report an orally available SARS-CoV-2 M^{pro} inhibitor with potent in vivo antiviral activity against wild-type (WT) and emerging variants of SARS-CoV-2.

Results

Discovery of SARS-CoV-2 M^{pro} inhibitors. To rapidly obtain lead compounds, we utilized the classical one-pot Ugi four-component reaction (Ugi-4CR, Fig. 1a)[22,23]. This reaction fuses a carboxylic acid (R-CO_2H), an amine (R^1-NH_2), an aldehyde (R^2-CHO) and an isocyanide (R^3-NC) to generate diamine derivatives with R, R^1, R^2 and R^3 linking the terminal acyl, the middle chiral carbon and amino nitrogen, and the terminal amino nitrogen, respectively. The Ugi-4CR has been previously adopted to produce non-covalent M^{pro} inhibitors[15,24]. Despite many efforts, the potency of generated diamine derivatives is still at the micromolar or sub-micromolar level[15,24]. Considering

[1]State Key Laboratory of Biotherapy and Cancer Center, West China Hospital, Sichuan University, Chengdu, Sichuan, China. [2]State Key Laboratory of Emerging Infectious Diseases, Carol Yu Centre for Infection, Department of Microbiology, Li Ka Shing Faculty of Medicine, The University of Hong Kong, Pokfulam, Hong Kong Special Administrative Region, China. [3]National Clinical Research Center for Geriatrics, West China Hospital, Sichuan University, Chengdu, Sichuan, China. [4]Department of Clinical Microbiology and Infection Control, The University of Hong Kong-Shenzhen Hospital, Shenzhen, Guangdong, China. [5]Academician workstation of Hainan Province and Hainan Medical University-The University of Hong Kong Joint Laboratory of Tropical Infectious Diseases, Hainan Medical University, Haikou, Hainan, China. [6]These authors contributed equally: Bao-Xue Quan, Huiping Shuai, An-Jie Xia, Yuxin Hou, Rui Zeng, Xin-Lei Liu, Gui-Feng Lin, Jing-Xin Qiao. ✉e-mail: jfwchan@hku.hk; leijian@scu.edu.cn; hinchu@hku.hk; yangsy@scu.edu.cn

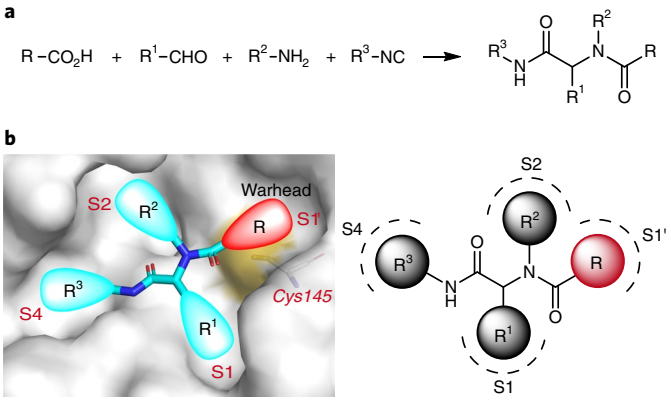

Fig. 1 | Schematic diagram of the design of SARS-CoV-2 M^{pro} inhibitors. **a**, The classical one-pot Ugi four-component reaction (Ugi-4CR). **b**, Fragments R, R^1, R^2 and R^3 in Ugi-4CR occupy the S1′, S1, S2 and S4 pockets of M^{pro}, respectively.

the advantages of covalent inhibitors in prolonging residence time and their ability to compete with high-affinity natural substrates[25], we decided to design covalent inhibitors on the basis of the Ugi-4CR.

According to the reported co-crystal structure of SARS-CoV-2 M^{pro} and diamines[15], fragments R, R^1, R^2 and R^3 occupy the S1′, S1, S2 and S4 pockets of M^{pro}, respectively (Fig. 1b). In the first step, we managed to find a proper electrophilic group (warhead) at the R position because it binds next to a cysteine residue (Cys145). To reduce potential toxicity, we chose warheads with mild or moderate electrophilicity. Here, α-ketoamide (R = acetyl) and acrylamide (R = vinyl) were selected as candidates because compounds carrying these warheads have been approved for use in the clinic[25], in addition to their lower reactivity. Two compounds ('1a' and '1b', Extended Data Fig. 1a) were synthesized with R being acetyl or vinyl, and R^1, R^2 and R^3 fixed as pyridine, tert-butylbenzene and tert-butyl, respectively, similar to groups in ML188, a non-covalent diamine derivative M^{pro} inhibitor[24]. Bioactivities of the two compounds against SARS-CoV-2 M^{pro} were determined by a fluorescence resonance energy transfer (FRET) assay and a differential scanning fluorimetry (DSF) assay. The α-ketoamide derivative '1a' (racemic mixture) showed good activity with a 50% inhibitory concentration (IC_{50}) of 3.11 μM in the FRET assay and a thermal shift (ΔT_m) of 4.7 °C in the DSF assay (Extended Data Fig. 1a). However, the acrylamide derivative '1b' displayed no activity (IC_{50} > 500 μM). A possible reason could be that the thiol of the Cys145 side chain prefers to react with the α-position carbon due to spatial location restriction, rather than the β-position carbon that is favoured in the common Michael addition reaction[15,16]. We then synthesized another 3 compounds with a bulkier α-ketoamide warhead, which exhibited substantially reduced activity (Extended Data Fig. 1a), implying that a bulky α-ketoamide warhead is not favourable. Therefore, the α-ketoamide with R = acetyl was finally selected as the warhead. Subsequently, racemic mixture '1a' was separated by chiral high performance liquid chromatography (HPLC). (*R*)-'1a' showed an IC_{50} of 2.38 μM, but (*S*)-'1a' displayed much weaker activity with an IC_{50} of 67.67 μM (Extended Data Fig. 1b). We solved the co-crystal structure of (*R*)-'1a'-M^{pro} (PDB entry 7FAY), which confirms the (*R*)-configuration of the active stereoisomer of '1a' (Extended Data Fig. 1c). Meanwhile, this co-crystal structure shows that the α-ketoamide group forms a covalent bond with Cys145, and pyridine (R^1), tert-butylbenzene (R^2) and tert-butyl (R^3), occupy the S1, S2 and S4 sites of M^{pro}, respectively, consistent with our expectation.

Then, a stepwise optimization of R^1, R^2 and R^3 of '1a' was carried out, which provided a number of optimal fragments with one fragment for R^1, four for R^2 and four for R^3 (Extended Data Fig. 2a and Supplementary Figs. 2–4). Although the pyrazinyl group at R^1 was found to have a better performance in improving potency (3f, Supplementary Fig. 3), it was not included because compounds containing this group at R^1 are unstable in alcohol solutions (Supplementary Fig. 5). To find better compounds, we further synthesized 16 compounds with various combinations of optimal fragments at R^2 and R^3 (Extended Data Fig. 2b). All these compounds showed potent activity against SARS-CoV-2 M^{pro}; they are epimeric mixtures due to the introduction of another stereocenter with a fixed *S*-configuration in R^3. The epimeric mixtures for these 16 compounds were subsequently separated by chiral HPLC. (*R*)-epimers (for simplicity, a simple nomenclature is used hereafter: (*R*)-/(*S*)-epimer, where (*R*)-/(*S*)- indicate the configurations of the chiral carbon linking the two amides) for all these compounds displayed much higher potency than the corresponding (*S*)-epimers. Among these compounds, (*R*)-'5b' showed the highest potency against M^{pro} with an IC_{50} of 11.3 nM. Again the (*S*)-epimer (*S*)-'5b' displayed weaker activity (IC_{50} = 751.9 nM). We then examined whether (*R*)-'5b' is prone to epimerization in vivo. Our results showed that the most active epimer (*R*)-'5b' could rapidly convert to the less active epimer (*S*)-'5b' in vivo (Extended Data Fig. 3); this could be due to the presence of an exchangeable hydrogen in the chiral carbon centre linking the two amides[26].

To prevent or reduce configuration conversion, we used deuterium to replace the exchangeable hydrogen. Deuterium has previously been explored to stabilize interconverting enantiomers, and has been shown to neither affect the pharmacological properties of a compound nor present a safety concern[27,28]. The generated compound, *d*-(*R*)-'6a' (a compound name with a '*d*-' prefix indicates deuterium other than hydrogen attached to the chiral carbon linking the two amines; Extended Data Fig. 4), showed similar potency as (*R*)-'5b'. Importantly, conversion from (*R*)- to (*S*)-epimers was substantially reduced (Extended Data Fig. 3). However, the PK properties of *d*-(*R*)-'6a' are poor, particularly the low oral bioavailability (10.1%) (Supplementary Table 1). We thus further optimized the chemical structure to improve oral bioavailability. A total of 11 compounds with deuterium were synthesized (Extended Data Fig. 4). All these compounds showed potent activity, with IC_{50} values ranging from 8.1 to 25.4 nM. The PK properties of these compounds were then evaluated in rats (Supplementary Table 1). Two compounds, *d*-(*R*)-'6c' and *d*-(*R*)-'6j', displayed good PK properties with oral bioavailabilities >30%. Because *d*-(*R*)-'6c' showed more potent activity than *d*-(*R*)-'6j' in both enzymatic (8.1 nM vs 20.4 nM, Extended Data Fig. 4) and cellular antiviral assays (Extended Data Fig. 5), *d*-(*R*)-'6c' (hereafter called Y180) was finally selected to carry out further evaluation; this compound also showed low conversion rate (from (*R*)- to (*S*)-epimers) in vivo (Extended Data Fig. 3).

As Y180 is a covalent inhibitor, we next determined the equilibrium-binding constant K_i and the inactivation rate constant k_{inac} to further verify its binding with M^{pro}. The measured K_i and K_{inac} values of Y180 are 1 nM and 2.6×10^{-4} s^{-1}, respectively (the corresponding values for PF-07321332, which is also a covalent M^{pro} inhibitor, are 2 nM and 5.1×10^{-4} s^{-1}, respectively, in the same assay; Supplementary Table 2). These data confirmed that Y180 is a potent M^{pro} inhibitor. Additionally, Y180 showed almost no activity against several common mammalian proteases with similar structure, including caspase 2, chymotrypsin, thrombin, cathepsin B, cathepsin D and cathepsin L (IC_{50} > 100 μM; Supplementary Table 3). Collectively, all these data indicate that Y180 is a potent and selective M^{pro} inhibitor.

Crystal structure of SARS-CoV-2 M^{pro} in complex with Y180. To illustrate the binding mode of M^{pro}-Y180, we determined the crystal structure of M^{pro} with Y180 at 2.1 Å (PDB entry 7FAZ). In this structure, two protomers per asymmetric unit form the biological dimer

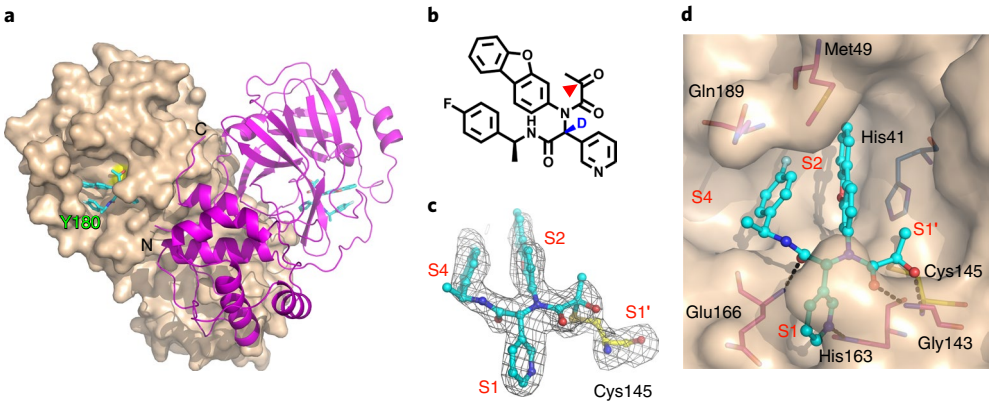

Fig. 2 | Overall structure of SARS-CoV-2 M^{pro} in complex with Y180. a, One protomer of the M^{pro} dimer is shown in surface view in wheat, the other displayed in cartoon view in magenta. The active site Cys145 is presented in yellow in the former protomer. Y180 in both molecules is shown with a stick model in cyan. The N and C termini of the cartoon-view protomer are labelled. **b**, The chemical structure of Y180. The warhead carbon is marked with a red triangle. Deuterium is shown in blue. **c**, The compound Y180 and Cys145 forming a covalent bond are displayed with a ball-and-stick model in cyan and yellow, respectively. *Fo* − *Fc* density map (σ = 2.5) is shown in grey. **d**, Detailed interactions of M^{pro} and Y180. Hydrogen bonds between them are shown as black dotted lines. The residues interacting with Y180 are labelled. **a**, **c** and **d** were prepared using PyMOL (https://pymol.org).

of M^{pro} (Fig. 2a). The detailed interaction mode of M^{pro} with Y180 is discussed below (Fig. 2b–d). The terminal carbonyl moiety (warhead) of inhibitor Y180 (Fig. 2b) forms a 1.8 Å covalent bond with the sulfur atom of catalytic residue Cys145 (Fig. 2c). The hydroxyl group of this thiohemiketal points into the traditional oxyanion hole stabilized by a hydrogen bond with the main-chain amide of Cys145 (Fig. 2d). In addition, the backbone amide of the residue Gly143 forms another hydrogen bond with the oxygen of the α-keto moiety. The dibenzo(b,d)furyl group of Y180 inserts deeply into the S2 pocket. Importantly, this dibenzo(b,d)furyl moiety displays parallel-displaced π-π stacking interactions with His41 and an intramolecular 4-fluorophenyl ring. Moreover, the dibenzo(b,d) furyl group is further stabilized through hydrophobic interactions with C_β of His41 and the side chain of Met49 (Fig. 2d). The pyridyl ring of inhibitor Y180 occupies the S1 pocket, forming a 2.9 Å hydrogen bond with a side chain of His163. Meanwhile, the backbone oxygen between the pyridyl ring and the 1-(4-fluorophenyl) ethyl group makes a hydrogen bond with the main-chain amide of Glu166. In the last moiety of Y180, the 4-fluorophenyl ring is stabilized through the π-π stacking interactions with the dibenzo(b,d) furyl group (mentioned above) and the hydrophobic interactions with C_ε of Met49, and the C_β and C_γ of Gln189.

Although M^{pro} is highly conserved in the emerging SARS-CoV-2 variants, there are still a number of mutated amino acids found in several variants (Supplementary Fig. 1), for example, Lys90Arg in B.1.351 (Beta), Lys90Arg and Ala193Val in B.1.351.2 (Beta), Lue205Val in P.2 (Zeta) and Pro132His in B.1.529 (Omicron). However, all these residues are far away from the Y180 binding site (>10 Å; see Supplementary Fig. 6), thus not affecting the inhibition efficiency of Y180 against M^{pro} (Supplementary Table 4).

In vitro antiviral activity of Y180. To evaluate the antiviral activity of Y180 in vitro, we used the VeroE6 cells stably expressing transmembrane serine protease 2 (VeroE6-TMPRSS2) and the human lung epithelial cell line, Calu3. The cells were challenged with WT SARS-CoV-2 and three other emerging variants B.1.1.7 (Alpha), B.1.617.1 (Kappa) and P.3 (Theta)[29]. Our data showed that Y180 did not cause observable cytotoxicity in VeroE6-TMPRSS2 and Calu3 cells within our treatment time frame (24 h) (Extended Data Fig. 6). Importantly, 20 μM Y180 decreased virus replication by 4.44-, 5.83-, 4.74- and 6.03-log against WT, B.1.1.7, B.1.617.1 and P.3, respectively, in VeroE6-TMPRSS2 cells at 24 h post infection (Fig. 3a–d). Similarly, Y180 at 20 μM demonstrated robust antiviral efficacy against SARS-CoV-2 in Calu3 cells with 2.14-, 3.13-, 1.77- and 2.29-log reduction of viral gene copies against SARS-CoV-2 WT, B.1.1.7, B.1.617.1 and P.3 variants, respectively (Fig. 3e–h). We next evaluated the efficacy of Y180 in inhibiting infectious virus progeny production with plaque reduction assays. Our results demonstrated that Y180 effectively reduced plaque formation of SARS-CoV-2 in both number and size, with EC_{50} of 11.4 nM, 20.3 nM, 34.4 nM and 23.7 nM against WT SARS-CoV-2, B.1.1.7, B.1.617.1 and P.3, respectively (Fig. 3i–l). To investigate whether suppression of virus replication would benefit the infection outcome of host cells, luciferase-based cell viability assay was carried out. Our results showed that Y180 substantially improved cell viability starting at 0.8 μM (Fig. 3m–p). At this concentration, Y180 demonstrated potent effects in protecting against SARS-CoV-2-induced cell death and the protection efficiency was higher than that of remdesivir (RDV) for WT (60.7% vs 43.9%, $P < 0.0001$), B.1.1.7 (106.6% vs 32.3%, $P < 0.0001$), B.1.617.1 (87.1% vs 14.6%, $P < 0.0001$) and P.3 (81.4% vs 67.1%, $P = 0.0136$). In addition to the comparison with RDV, we similarly side-by-side compared the Y180 antiviral efficacy with that of PF-07321332. When compared with the mock-treated control, Y180 effectively reduced viral titre by 5.7-log at 0.8 μM, while PF-07321332 decreased the viral load by 0.2-log at this concentration (Y180 vs PF-07321332, $P < 0.0001$; Extended Data Fig. 7). We further tested the efficacy of Y180 against the B.1.1.529 (Omicron) variant in vitro. Y180 decreased B.1.1.529 viral gene copies by 3.92-log at 20 μM compared with the vehicle control (Extended Data Fig. 8). Together, our data demonstrated that Y180 rendered superb cross-protection against WT and different emerging SARS-CoV-2 variants, including the latest Omicron variant, by potently abolishing virus replication.

Evaluation of PK properties and safety of Y180. Before evaluating the in vivo PK properties of Y180, we first measured its lipid/water partition coefficient (logP), apparent permeability coefficients (P_{app}), water solubility and in vitro metabolic stability in human liver microsomes. The measured logP/ P_{app}/solubility values of Y180 are $2.35/1.52 \times 10^{-6}$ (cm s^{-1})/3.06 (μg ml^{-1}) (the corresponding values of PF-07321332 are $0.91/0.58 \times 10^{-6}$ (cm s^{-1})/5.72 (μg ml^{-1}); Supplementary Table 5), indicating low water solubility (without any auxiliary materials as solubilizer) and good membrane permeability. Since ritonavir was recently reported to increase the

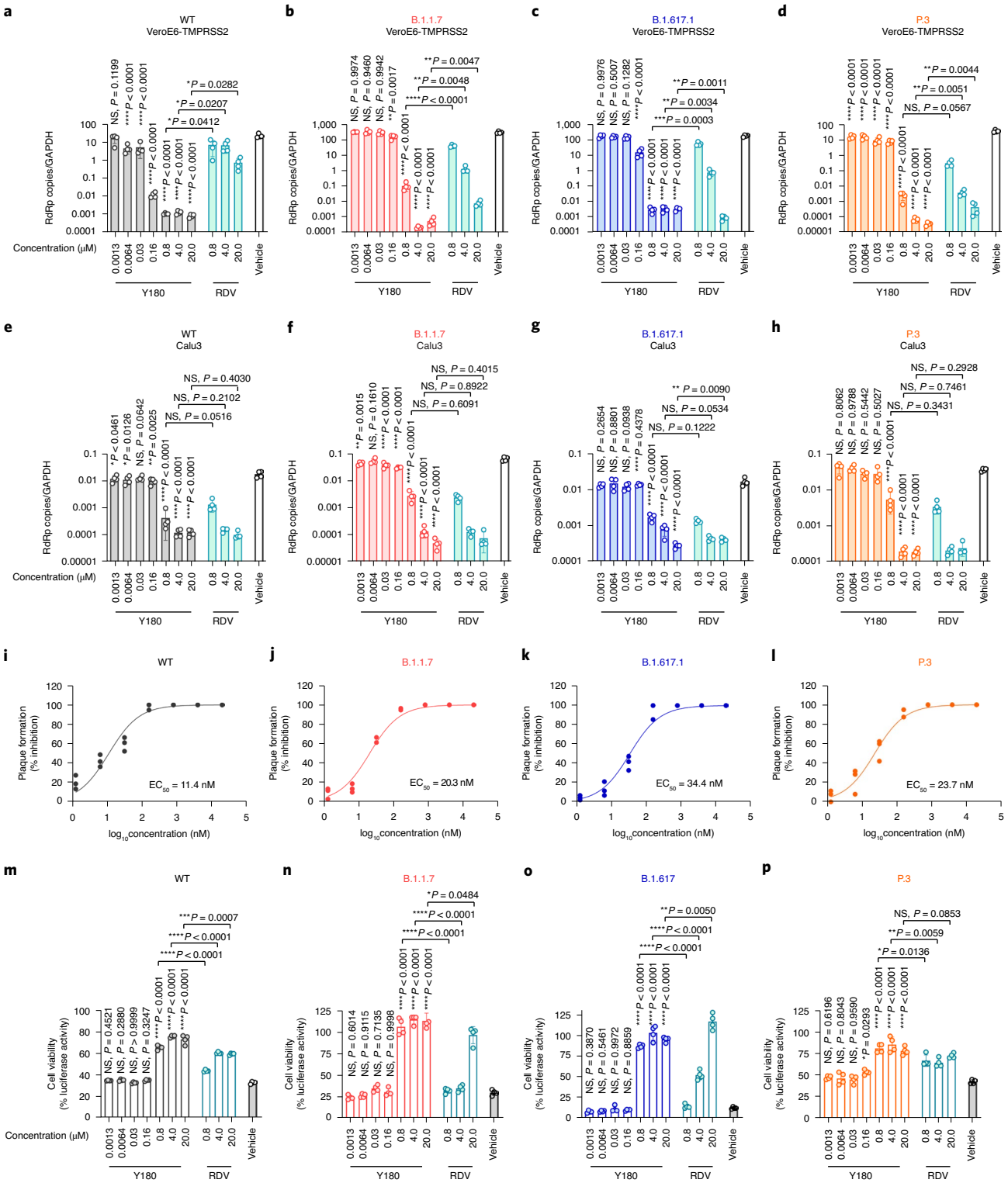

Fig. 3 | Evaluation of in vitro antiviral activity of Y180. a–d VeroE6-TMPRSS2 cells were infected with SARS-CoV-2 at 0.01 MOI. Lysates were collected at 24 h.p.i. for the detection of viral titre with RT-qPCR ($n = 4$). Viral RNA-dependent RNA polymerase (RdRp) gene copies in VeroE6-TMPRSS2 infected with WT (**a**), B.1.1.7 (**b**), B.1.617.1 (**c**) and P.3 (**d**). **e–h**, Calu3 cells were infected with SARS-CoV-2 at 1 MOI. Lysates were collected at 24 h.p.i. for the detection of viral titre with RT-qPCR ($n = 4$). Viral RdRp gene copies in cells infected with WT (**e**), B.1.1.7 (**f**), B.1.617.1 (**g**) and P.3 (**h**). **i–l**, VeroE6-TMPRSS2 cells were infected with 50–70 PFU SARS-CoV-2 followed by Y180 addition at 2 h.p.i. and fixation at 48 h.p.i. ($n = 3$). Plaque formation was counted in cells infected with WT (**i**), B.1.1.7 (**j**), B.1.617.1 (**k**) and P.3 (**l**). Inhibition of plaque formation was normalized to vehicle controls. **m–p**, VeroE6-TMPRSS2 cells were infected with SARS-CoV-2 at 1 MOI. Cell viability was determined at 48 h.p.i. by measuring luciferase activity in cells ($n = 4$) infected with WT (**m**), B.1.1.7 (**n**), B.1.617.1 (**o**) and P.3 (**p**). Luciferase readings were normalized to mock-treated controls without virus infection. Data were obtained from three independent experiments. All data are shown as mean ± s.d. Statistical significance was assessed by one-way ANOVA compared with the vehicle control group; Student's *t*-test compared with RDV treatment group. $^{*}P < 0.05$, $^{**}P < 0.01$, $^{***}P < 0.001$, $^{****}P < 0.0001$; NS, not significant.

stability of PF-07321332[17] in vivo, we examined whether the pharmacokinetic metabolism of Y180 can also be improved by ritonavir co-administration. To this end, we performed the human liver microsome assay. The data suggested that the half-life of Y180 was substantially increased from 13.86 min to >120 min by ritonavir co-administration (Supplementary Table 6).

Next, the in vivo PK properties of Y180 were evaluated. Y180 displayed satisfying PK properties in mice, rats and dogs, with oral bioavailabilities of 92.9%, 31.9% and 85.7%, respectively (Supplementary Tables 1 and 7). Since mice were used in the subsequent in vivo animal experiments, key PK parameters of Y180 in mice are summarized as follows. When administered orally (p.o.) (150 mg kg^{-1}), Y180 showed an area under the curve (AUC) value of 29,201 h×ng ml^{-1}. It displayed a half-life ($T_{1/2}$) of 1.42 h and an oral bioavailability of 92.9%. On the basis of the EC_{50}/EC_{90} values from B.1.1.7- or B.1.617.1-infected VeroE6-TMPRSS2 cells (Fig. 3j,k), a single oral (p.o.) dose of 150 mg kg^{-1} d^{-1} Y180 maintained the plasma levels at EC_{50} (20.3 nM) or EC_{50} (34.4 nM), and EC_{90} (73.1 nM) or EC_{90} (157.0 nM) for about 18 or 16 h, and 11 or 12 h, respectively (Extended Data Fig. 9). In vitro cytotoxicity of compound Y180 and (*S*)-'6c' ((*S*)-epimer, without deuterium) (Supplementary Fig. 7), a potential configuration conversion product of Y180, was evaluated by the 3-(4,5-dimethylthiazol-2-yl)-2,5-diphenyltetrazolium bromide (MTT) assay in various cell lines, including A549, VeroE6, Huh7, BEAS-2B and HUVEC. Both compounds showed low cytotoxicity in these cell lines (Supplementary Table 8). Preliminary in vivo toxicity of Y180 and (*S*)-'6c' was then evaluated in rats. In an acute toxicity experiment, no rats died after p.o. treatment with 600 mg kg^{-1} of Y180 or (*S*)-'6c' (Supplementary Table 9). In a repeated-dose toxicity study, treatment with p.o. Y180 or (*S*)-'6c' at 400 mg kg^{-1} twice daily for 7 consecutive days did not result in notable body weight change or pathological changes in heart, liver, lung, kidney and spleen (Extended Data Fig. 6e,f), suggesting no toxicity of Y180 and (*S*)-'6c' in rats at therapeutic concentrations.

In vivo antiviral activity of Y180. Finally, we evaluated the in vivo antiviral efficacy of Y180 against B.1.1.7 and B.1.617.1 variants in an established K18-human angiotensin-converting enzyme 2 (K18-hACE2) transgenic mouse model. Compared with other currently available small-animal models for COVID-19, the K18-hACE2 mouse model supports robust SARS-CoV-2 replication with lethal outcome[30–32], which makes it a stringent model for the evaluation of drug candidates in ameliorating severe SARS-CoV-2 infection. Y180 was orally administered to the mice starting from 1 h before infection and 6 h post infection (h.p.i.) in the prophylactic group and therapeutic group, respectively (Fig. 4a). In the B.1.1.7-infected K18-hACE2 mice, prophylactic Y180 significantly decreased viral gene copies in the nasal turbinate by 12.0- ($P<0.0001$) and 31.5-fold ($P<0.0001$) at 2 d.p.i. and 4 d.p.i. compared with the vehicle group, respectively (Fig. 4b). Similarly, even when treatment was postponed to begin at 6 h.p.i., therapeutic administration of Y180 effectively inhibited virus replication, as evidenced by 3.3- ($P<0.0001$) and 5.4-fold ($P<0.0001$) decrease in nasal turbinate viral gene copies at 2 d.p.i. and 4 d.p.i. (Fig. 4b). In addition, virus replication in the lung was also inhibited by Y180 treatment, with decreases in viral gene copies ranging from 2.7- to 8.8-fold (Fig. 4c). Consistent with the findings in viral gene copies, infectious viral titres in both the lung and the nasal turbinate of Y180-treated mice were substantially diminished compared with the vehicle group (Fig. 4d,e). In agreement with these observations, both prophylactic and therapeutic Y180 significantly ameliorated the expression of representative virus-induced pro-inflammatory cytokines, including interferon gamma (IFNγ) and interferon-inducible protein 10 (IP10) (Fig. 4f). Next, immunohistochemistry assays revealed that abundant expression of viral antigen was identified in both lung and nasal turbinate of the mock-treated mice at 2 d.p.i. (Fig. 4g, black arrows). In contrast, Y180 treatment, even when administered after virus challenge, markedly suppressed viral nucleocapsid protein expression in both lung and nasal turbinate (Fig. 4g). To examine whether Y180 treatment contributed to alleviating disease severity in the transgenic mice, we performed hematoxylin-eosin (H&E) staining to assess virus-induced tissue damage in both lung and nasal turbinate. In the lung of vehicle-treated mice, severe inflammatory infiltrations were frequently observed in the alveoli and alveoli septa, leading to alveolar congestion at 2 d.p.i. (Fig. 4h, vehicle, enlarged image 1, yellow arrowheads). In the small airways, debris of necrotic epithelium was detected in the bronchiole cavities (Fig. 4h, vehicle, enlarged image 2, yellow arrowheads). In the blood vessels, mononuclear cell infiltrations in the endothelium were observed (Fig. 4h, vehicle, enlarged image 3, yellow arrowheads). In sharp contrast, the overall histological architecture of mice receiving either prophylactic or therapeutic Y180 treatment was remarkably preserved (Fig. 4h), except for mild infiltrations of inflammatory cells in the alveolar septa. Consistently, severe tissue damage, including loss of integrity of the nasal epithelium, haemorrhage in the lamina propria and necrotic cells in the nasal cavities, were detected in the nasal turbinate of vehicle-treated mice, while morphology of these tissues in the Y180-treated mice remained largely intact at 2 d.p.i. (Fig. 4h). Since our data demonstrated that Y180 is effective against multiple SARS-CoV-2 variants, we performed additional in vivo experiments with B.1.617.1 to evaluate the infection outcome of K18-hACE2 transgenic mice upon lethal

Fig. 4 | Evaluation of in vivo antiviral activity of prophylactic and therapeutic Y180 in the lethal K18-hACE2 transgenic mouse model for COVID-19. **a**, Schematic illustration of experiment design. K18-hACE2 transgenic mice were challenged with either 250 PFU B.1.1.7 or 1×10^5 PFU B.1.617.1. Oral administration of either 150 mg kg^{-1} dose^{-1} Y180 or vehicle solution was performed twice daily (bis in die; b.i.d.) for 8 d or until death, whichever was earlier. For mice with prophylactic treatment, Y180 treatment was initiated at 1 h before virus challenge, whereas administration of Y180 was postponed until 6 h.p.i. for mice receiving therapeutic treatment. **b**,**c**, Mice infected with B.1.1.7 were killed at 2 d.p.i. and 4 d.p.i. for detection of viral RdRp gene copies in nasal turbinate (**b**) and lung (**c**) by RT–qPCR ($n=5$ at 2 d.p.i.; $n=6$ at 4 d.p.i.). **d**,**e**, Mice infected with B.1.1.7 were killed at 2 d.p.i. and 4 d.p.i. for detection of infectious viral titre in nasal turbinate (**d**) and lung (**e**) by plaque assay ($n=5$ at 2 d.p.i.; $n=6$ at 4 d.p.i.). **f**, Gene expression of IFNγ and IP10 in the lung of mice infected with B.1.1.7 at 4 d.p.i. were determined with RT–qPCR ($n=5$ at 2 d.p.i.; $n=6$ at 4 d.p.i.). **g**, Immunohistochemistry staining visualizing the nucleocapsid protein (brown, indicated by black arrows) in the lung and nasal turbinate of mice infected with B.1.1.7 at 2 d.p.i. Scale bar, 100 μm. **h**, Histology analysis visualizing the virus-induced pathology in the lung and nasal turbinate of mice infected with B.1.1.7 at 2 d.p.i. Representative images of alveoli, bronchioles and blood vessels of the lung are indicated by yellow dotted circles with numbers, and enlarged in images 1, 2 and 3, respectively. Yellow arrowheads indicate inflammatory infiltrations in the alveoli, dead cell debris in the bronchioles and mononuclear cell infiltrations in the blood vessels in the enlarged images 1–3. Black arrowheads, haemorrhage; black arrows, epithelium detachment; #, dead cell debris. Scale bar, 100 μm for enlarged images 1–3, 200 μm for nasal turbinate image. Three mice were sampled in each group and 4–6 sections from each animal were used for histology analysis. **i**,**j**, Mice challenged with 1×10^5 PFU B.1.617.1 were treated with either 150 mg kg^{-1} dose^{-1} Y180 or vehicle solution twice daily ($n=8$–9). Survival (**i**) and body weight (**j**) of mice were monitored daily until 14 d.p.i. Data were obtained from two independent experiments. All data are shown as mean ± s.d. Statistical differences were determined by two-way ANOVA in **b**–**e** and **j**, one-way ANOVA in **f** or log-rank (Mantel-Cox) test in **i**. *$P<0.05$, **$P<0.01$, ***$P<0.001$, ****$P<0.0001$.

SARS-CoV-2 infection. Our results showed that Y180 treatment significantly improved the survival of mice against B.1.617.1 infection (Fig. 4i; vehicle: 0 of 8 or 0% vs prophylactic treatment: 2 of 9 or 22.2% vs therapeutic treatment: 4 of 9 or 44.4%; $P=0.0402$ and $P=0.0086$, respectively). Corroborating the survival findings, Y180 also significantly improved the body weight of B.1.617.1-infected mice starting from 4 d.p.i. (Fig. 4j).

Moreover, we performed head-to-head comparison to evaluate the antiviral efficacy of Y180/ritonavir and PAXLOVID (PF-7321332/ritonavir), the FDA-approved orally available M^{pro} inhibitor, against B.1.1.529 infection. Our data demonstrated that therapeutic treatment with Y180/ritonavir potently reduced viral RdRp gene copies by 14.9-fold ($P=0.0429$) and 27.7-fold ($P=0.0056$) in nasal turbinate and lung, respectively, of the infected mice at 2 dpi. (Extended

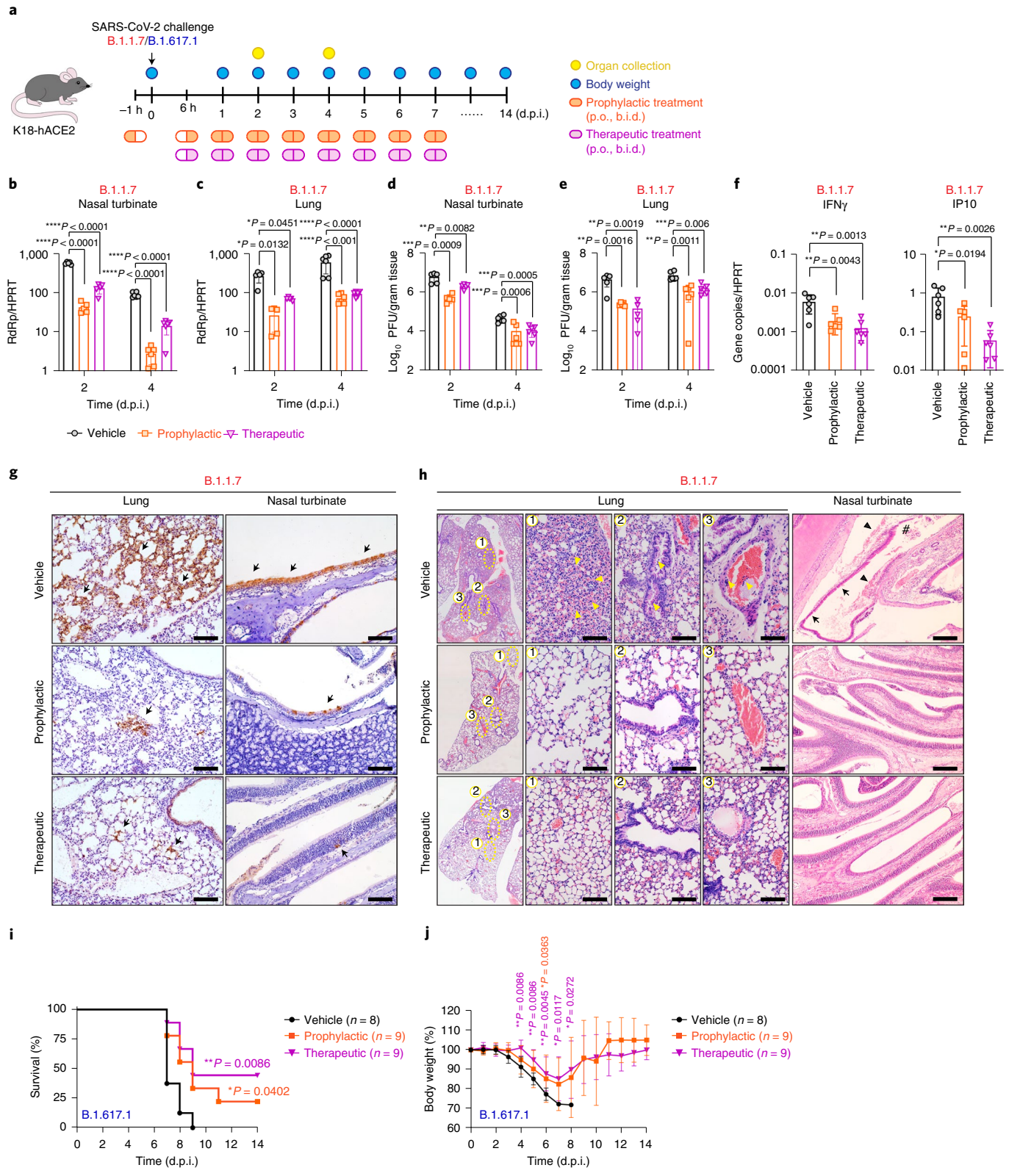

Data Fig. 10a,b). In comparison, PF-07321332/ritonavir reduced viral gene copies by 0.8-fold (P=NS) and 14.1-fold (P=0.0070) in nasal turbinate and lung, respectively, under the same therapeutic conditions (Extended Data Fig. 10a,b). Similarly, Y180/ritonavir suppressed the production of infectious viral progenies in lung more efficiently than PF-07321332/ritonavir (Extended Data Fig. 10c). Therefore, our data suggested that the in vivo antiviral efficacy of Y180/ritonavir combined treatment is more potent than that of PF-07321332/ritonavir in the K18-hACE2 mouse model. Collectively, our results demonstrate that Y180 is highly effective against WT SARS-CoV-2 and emerging SARS-CoV-2 variants including Omicron both in vitro and in vivo by reducing virus replication, which results in an attenuated disease severity and improves the host survival outcomes upon SARS-CoV-2 infection.

Discussion

The emergence of SARS-CoV-2 variants heavily increased the challenges for curbing the COVID-19 pandemic. For example, the B.1.1.7, B.1.617.1, P.3 and the recently emerged B.1.1.529 variants[2] were shown to have enhanced transmissibility and/or ability to escape from currently available vaccines and therapeutic monoclonal antibodies[1–3], which target the spike protein. Effective antivirals targeting the M^{pro}, which is highly conserved among different SARS-CoV-2 variants, is an effective strategy to deal with this challenging task.

In this study, to discover M^{pro} inhibitors with potential for rapid translation into clinical application, we designed a series of diamide derivatives, which can be easily synthesized using Ugi-4CR. In our designed compounds, we introduced an acetyl group at the terminal acyl of the amide, which allowed the formation of an α-ketoamide warhead in the S1′ pocket. Further, to reduce configuration conversion of the most active epimer ((*R*)-epimer) to its less active epimer (*S*-configuration), deuterium was used to replace the exchangeable hydrogen attached to the chiral carbon linking the two amides.

The selected compound Y180 showed potent SARS-CoV-2 M^{pro} inhibitory activity with an IC_{50} of 8.1 nM. Importantly, the introduction of deuterium at the chiral carbon substantially reduced configuration conversion of Y180 from the active (*R*)-epimer to the less active (*S*)-epimer. Y180 displayed good PK properties in mice, rats and dogs, with oral bioavailabilities of 92.9%, 31.9% and 85.7%, respectively. It displayed outstanding in vitro antiviral potency against WT SARS-CoV-2 and the B.1.1.7, B.1.617.1, P.3 and B.1.1.529 variants. Importantly, Y180 demonstrated remarkable in vivo antiviral potency and improved the disease outcome against B.1.1.7, B.1.617.1 and B.1.1.529 infection both prophylactically and therapeutically as evidenced by the significantly decreased viral burden, attenuated tissue damage and improved survival among the infected animals. Together, our data provided strong evidence for the therapeutic potential of Y180 against SARS-CoV-2 infection in a lethal infection model.

Compared with other reported M^{pro} inhibitors[9–21], Y180: (1) is the most potent non-peptidomimetic M^{pro} inhibitors reported thus far, inhibiting SARS-CoV-2 M^{pro} activity at single-digit nanomolar ranges, (2) demonstrates the best EC_{50} values against WT SARS-CoV-2 and its variants at low double-digit nanomolar ranges in vitro and (3) is the only reported orally administered M^{pro} inhibitor that can rescue the survival of animals upon infection with SARS-CoV-2 variants in a lethal COVID-19 mouse model. Importantly, in a head-to-head in vivo antiviral assay, therapeutic treatment with Y180/ritonavir was more potent than PF-07321332/ritonavir against SARS-CoV-2 Omicron in K18-hACE2 transgenic mice. Meanwhile, the simplicity of the chemical synthesis of Y180 is also unrivalled compared with that of PF-07321332, which is a peptidomimetic M^{pro} inhibitor. As a covalent inhibitor, the safety of Y180 may be of concern. However, Y180 has obvious safety advantages because: (1) it contains a mild warhead, α-ketoamide, which reduces toxicity (a number of compounds containing α-ketoamide warheads have been approved for clinical use, such as antivirals against hepatitis C virus (HCV) infection, Boceprevir, Telaprevir and Narlaprevir); (2) it showed excellent selectivity for M^{pro} compared with other common mammalian proteases with similar structure (see Supplementary Table 3); and (3) in our preliminary preclinical safety evaluation, Y180 did not show obvious toxicity both in vitro and in vivo. Of course, the safety of Y180 in humans remains to be determined in clinical trials. Collectively, we identified an orally available M^{pro} inhibitor that demonstrated potent in vitro and in vivo antiviral activity against WT SARS-CoV-2 and emerging variants. Our work advances the development of highly specific antiviral therapeutics against COVID-19.

Methods

Cell lines. Huh7 (Cell Bank, Chinese Academy of Sciences, Shanghai, SCSP-526), BEAS-2B (Cell Bank, Chinese Academy of Sciences, Shanghai, GNHu27), A549 (ATCC, CRM-CCL-185), HUVEC (CCTCC, Wuhan, GDC0635), VeroE6 (ATCC, CRL-1586) and VeroE6-TMPRSS2 (JCRB 1819) cells were maintained in Dulbecco's modified Eagle medium (DMEM, Gibco) supplemented with 10% heat-inactivated foetal bovine serum (FBS), 100 U ml^{-1} penicillin and 100 μg ml^{-1} streptomycin. Calu3 cells (ATCC, HTB-55) were maintained in DMEM/F12 supplemented with 10% heat-inactivated FBS, 100 U ml^{-1} penicillin and 100 μg ml^{-1} streptomycin.

Viruses. SARS-CoV-2 HKU-001a (GenBank accession number MT230904), B.1.1.7 (GISAID: EPI_ISL_1273444), B.1.617.1 (GISAID: EPI_ISL_2423557), P.3 (GISAID: EPI_ISL_1660475) and B.1.529 (GenBank accession number OM212472) were isolated from laboratory-confirmed COVID-19 patients in Hong Kong[33]. WT SARS-CoV-2 and its variants were cultured in VeroE6-TMPRSS2 and titrated by plaque assays. All infectious experiments followed the approved standard operating procedures of the Biosafety Level 3 facility at the Department of Microbiology, HKU.

Production of authentic SARS-CoV-2 and Omicron variant's main protease. Using the wild-type SARS-CoV-2 (GenBank: MN908947.3) pET28b-main protease (M^{pro}) plasmid[13] as template, SARS-CoV-2 Omicron variant (B.1.1.529, GISAID accession ID: EPI_ISL_6590782.2) M^{pro} (Pro132His mutation) was obtained by site-directed mutagenesis PCR using the two primers: 5'-GCAATGCGTC*AT*AATTTTACCATTAAGGGTAGTTTTCTG-3' and 5'-GGTAAAATT*AT*GACGCATTGCACACTGATAAACGCC-3' (mutated codons shown in italic). The PCR products were then digested by DpnI (TakaRa) and directly transformed to *Escherichia coli* DH5α competent cells (Novagen). The positive clones were incubated in Luria broth medium overnight and the corresponding plasmids were extracted using the Omega E.Z.N.A. Plasmid Mini Kit I (Omega Bio-Tek). All DNA plasmids were sequenced and the correctness of the Pro132His mutation was verified. Subsequently, the WT SARS-CoV-2 or omicron variant pET28b-M^{pro} plasmid was expressed in *E. coli* BL21(DE3) cells (Novagen). The cell pellets were resuspended in buffer A (20 mM Tris-HCl pH 8.0, 10 mM imidazole, 500 mM NaCl and 5% glycerol), lysed via ultrasonication on ice and centrifuged at 38,759×*g* at 4 °C. The supernatants were loaded onto HisTrap FF column (GE Healthcare) and eluted with buffer B (20 mM Tris-HCl pH 8.0, 500 mM imidazole, 500 mM NaCl and 5% glycerol). The target protein (wild-type or Omicron variant M^{pro}) was processed by PreScission protease at 4 °C overnight to remove the His-tag. The mixture was loaded onto GSTrap FF (GE Healthcare) and HisTrap FF columns again to remove PreScission and uncleaved M^{pro}. The target protein was further purified by gel filtration (Superdex 75 Increase 10/300 GL, GE Healthcare) in buffer C (20 mM Tris-HCl pH 8.0, 150 mM NaCl). The quality of the purified wild-type or Omicron variant M^{pro} was checked by SDS–PAGE.

Crystallization of SARS-CoV-2 M^{pro} in complex with (*R*)-1a or Y180. The SARS-CoV-2 M^{pro} was concentrated to ~5 mg ml^{-1} and incubated with each compound at a molar ratio of 1:10 at 4 °C overnight. Subsequently, crystallization was performed at 291 K using the sitting-drop vapour-diffusion method by mixing 1 μl protein solution plus 1 μl reservoir to equilibrate against 70 μl reservoir solution. The commercial screen kits—Index, Crystal Screen 1/2 (Hampton Research) and JBScreen Basic 1-4 (Jena Bioscience)—were used. The crystals of M^{pro}-(*R*)-'1a' were obtained within 5 d under condition No. 80 of Index: 0.2 M ammonium acetate, 0.1 M HEPES pH 7.5, 25% w/v PEG3350. The crystals of M^{pro}-Y180 were obtained within 3 d under condition No. 22 of Crystal Screen 1/2: 0.2 M sodium acetate trihydrate, 0.1 M TRIS hydrochloride pH 8.5, 30% w/v PEG4000. All crystals were flash-cooled in liquid nitrogen with cryo-protectant solution (50% w/v PEG3350).

Data collection, phase determination and refinement. The diffraction datasets of both M^{pro}-(*R*)-'1a' and M^{pro}-Y180 were collected at an X-ray wavelength 0.97852 Å at Shanghai Synchrotron Radiation Facility (SSRF) beamline BL19U1 (Shanghai,

China). The dataset of M^{pro}-(*R*)-'1a' was processed at a resolution of 2.1 Å and in space group 'C2' by 'XDS'[34], and scaled with 'Aimless'[35] in CCP4. The dataset of M^{pro}-Y180 was also processed at a resolution 2.1 Å, but with space group '$P2_12_12_1$'. The initial phases of the SARS-CoV-2 M^{pro} was determined by molecular replacement method with the programme PHASER[36], using the M^{pro} structure from PDB entry 7D3I[13] as the search model. Compound (*R*)-'1a' or Y180 was then built into the model using the programme 'Coot'[37]. Refinement of the complex M^{pro}-(*R*)-'1a' was performed using 'BUSTER'[38], while refinement of M^{pro}-Y180 was processed using 'Phenix REFINE'[39]. In the final structure of M^{pro}-(*R*)-'1a' or M^{pro}-Y180, >97% of residues are in the preferred regions of the 'Ramachandran plot' statistics. The statistics of the diffraction dataset and the final refinement are presented in Supplementary Table 10.

Enzyme kinetics, correction of inner-filter effect, IC_{50}, K_i and k_{inac} measurements. Enzyme kinetics assay was performed in 20 mM HEPES buffer, 120 mM NaCl, 0.4 mM EDTA, 4 mM dithiothreitol and 20% glycerol at pH 6.5. The reaction was initiated by adding 25 µl of the MCA-AVLQSGFR-Lys(DNP)-Lys-NH2 fluorescent substrate (1.6~200 µM) into 25 µl of the WT SARS-CoV-2 or Omicron variant M^{pro} (final concentration: 100 nM). The fluorescence signal of unquenched MCA was monitored at emission/excitation wavelengths of 405/320 nm using a CLARIOstar microplate reader (BMG Labtech). The initial velocities were calculated from the linear section of the reaction curves and the amounts of the cleaved substrate were obtained by fitting the fluorescence to a calibration curve of free MCA (0.01~20 µM).

The inner-filter effect of the fluorescent substrate was corrected. The measured fluorescence values of background and substrate with different concentrations were defined as *f*(0) and *f*(S). Free MCA (final concentration: 0.5 µM) was then added into each well. The second fluorescence measurements were taken as *f*(0+MCA) and *f*(S + MCA). The inner-filter effect of the substrate was corrected according to the equation

$$\mathrm{Corr}\% = 100\% \times \frac{f(\mathrm{S} + \mathrm{MCA}) - f(\mathrm{S})}{f(0 + \mathrm{MCA}) - f(0)}.$$

The corrected initial velocity of the reaction in the enzyme kinetics assay was calculated as

$$V = V_{\text{initial velocity}}/(\mathrm{Corr}\%).$$

For the determination of IC_{50} values, 22.5 µl of the recombinant authentic WT SARS-CoV-2 or Omicron variant M^{pro} (final concentration: 100 nM) was pre-incubated with 2.5 µl of various concentrations of each compound for 10 min. Then the reaction was initiated by adding 25 µl of the fluorescent substrate (final concentration: 20 µM) and monitored at 405 nm with excitation at 320 nm in the kinetic mode using the CLARIOstar microplate reader (BMG Labtech). The initial velocities were calculated from the linear section of the reaction curves. The IC_{50} values were calculated using a dose-response model in GraphPad Prism 8.0 software.

In the inhibition constant (K_i) assay, 22.5 µl of the M^{pro} (final concentration: 100 nM) was mixed with 2.5 µl of various concentrations (4.9~312.5 nM) of Y180 or PF-07321332. The reactions were immediately initiated by adding 25 µl of the fluorescent substrate (final concentration: 30 µM). The fluorescence signal was monitored using CLARIOstar microplate reader (BMG Labtech). The initial velocities were calculated from the linear section of the reaction curves. The K_i values for compounds Y180 and PF-07321332 were determined with the Morrison equation in GraphPad Prism 8.0 software.

In the inactivation rate constant (k_{inac}) assay, 22.5 µl of the M^{pro} (final concentration: 100 nM) was mixed with 2.5 µl of different concentrations (3.3~25.0 nM) of Y180 or PF-07321332. The reactions were monitored by addition 25 µl of the fluorescent substrate (final concentration: 20 µM) for 15 min. The observed first-order rate constant k_{obs} was obtained by fitting the progress curves of different concentrations of inhibitor to the one-phase association equation in GraphPad Prism 8.0 software. The constant $k_{obs}/[I]$ ($[I]$ is the concentration of the inhibitor) was obtained by linear regression analysis. The mimic k_{inac} value was calculated using the equation[40]

$$k_{\mathrm{inac}}/K_{\mathrm{i}} = \left(1 + \frac{[S]}{K_{\mathrm{m}}}\right) \times k_{\mathrm{obs}}/[I].$$

Differential scanning fluorimetry assay. Differential scanning fluorimetry assays were performed using BioRad CFX96 real-time PCR detection system. M^{pro} was added to a final concentration of 2 µM and incubated with 40 µM test compounds for 30 min. Orange dye (5×SYPRO, Sigma) was added and the thermal denaturation was measured with a temperature gradient of 1.5 °C min^{-1} from 20 °C to 95 °C. The melt temperature (T_m) was calculated by using a Boltzmann model in GraphPad Prism 8.0 software. The thermal shift (ΔT_m) was calculated using the equation $\Delta T_m = T_{m(\text{compound})} - T_{m(\text{DMSO})}$. All experiments were performed in triplicate, and the values are presented as mean ± s.d.

Biochemical activity assay against mammalian proteases. The biochemical activity against mammalian proteases was determined by Human Proteases assay kit (Biovision) and performed following the manufacturer's instructions. All experiments were performed in triplicate.

Cytotoxicity assay. For VeroE6, HUVEC, A549, BEAS-2B and Huh7 cells, cells were seeded in 96-well plates and grown overnight. Various concentrations (0.41~100 µM) of Y180 or (*S*)-**6c** were then added to each well. After incubation for 48 h, cell viability was evaluated using MTT (Sigma) according to the manufacturer's protocol. All experiments were performed in triplicate.

For VeroE6-TMPRSS2 and Calu3 cells, cells were treated with either Y180 in 5-fold serial dilution, ranging from 0.0013 µM to 500 µM, or with vehicle (dimethyl sulfoxide; DMSO) for 72 h. Cell viability was quantified by CellTiter-Glo luminescent cell viability assay kit (G7572, Promega) following the manufacturer's instructions, with a multilabel plate reader Victor X3 (Perkin Elmer)[41].

PK properties and chiral inversion in vivo. All procedures related to animal handling, care and treatment in PK studies were performed according to approved guidelines. The PK studies were approved by the Ethics Committee of Shanghai Medicilon Inc., ZLA (Beijing) Pharmaceutical Technology Co. Ltd. and Sichuan Greentech Biotechnology Co. Ltd. All animals used in this study were chosen randomly.

In PK properties and chiral inversion studies, compounds, doses and administration schemes are shown in Supplementary Tables 1 and 7. Briefly, male Sprague Dawley (SD) rats, male ICR (Institute of Cancer Research) mice or beagle dogs ($n = 3$ per group, aged 1~2 yr and weighing 9~12 kg) were treated with the test compounds at the indicated doses by oral gavage or intravenously. In the case of the male SD rats, the compounds were dissolved in 10% DMSO, 40% PEG300, 5% Tween-80 and 45% saline. As for the ICR mice and beagle dogs, the compounds were dissolved in 10% DMSO, 42% PEG300, 3% polyethylene-polypropylene glycol and 45% saline.

Blood samples were collected at 0.083, 0.25, 0.5, 1, 2, 4, 6, 8 and 24 h after administration. Serum samples were obtained by centrifugation and the concentrations of compounds in the serum were analysed by liquid chromatography tandem mass spectrometry (LC–MS/MS) (Agilent 1200 series HPLC (Agilent) coupled to an API4000 mass spectrometer (Applied Biosystems/MDS Sciex)). The PK parameters were calculated using Phoenix WinNonlin7.0.

Serum samples from rats at 0.25, 1 and 6 h were selected to evaluate chiral inversion of the compounds in vivo by LC–MS/MS. The LC–MS/MS separation of *R*- and *S*-epimers of compounds was performed on a Lux Cellulose 3 chiral column (4.6 × 250 mm, 5.0 µm particle size) and the percentage of *S*-epimers was used to estimate the degree of chiral conversion.

Metabolic stability in human liver microsomes (HLM). Test compound (Y180, Y180 with Ritonavir, PF-07321332 or PF-07321332 with Ritonavir) incubations were conducted with 0.5 mg ml^{-1} human liver microsomes at 37 °C open to ambient air at various timepoints (0, 5, 15, 35, 45 and 60 min). Samples were collected and analysed by LC–MS/MS. The substrate depletion half-life ($T_{1/2}$) and intrinsic clearance (CL_{int}) were calculated using: $T_{1/2} = 0.693/K$ (K is the rate constant from a plot of ln[concentration] vs incubation time) and $CL_{int} = (0.693/T_{1/2}) \times \{1/[\text{microsomal protein concentration (0.5 mg } ml^{-1})]\} \times$ scaling factors (1,254.2).

In vivo toxicity study. All procedures related to animal handling, care and treatment in in vivo toxicity studies were performed according to approved guidelines. This study was approved by the Ethics and Animal Welfare Committee of West China Hospital, Sichuan University (20211063A). All animals used in this study were chosen randomly.

SD rats (aged 7–11 weeks) consisted of half male (weight: 200–230 g) and half female (weight: 190–220 g) were used to assess toxicity of Y180 and (*S*)-'6c' in vivo. Compounds were dissolved in 10% DMSO, 42% PEG300, 3% polyethylene-polypropylene glycol and 45% saline.

Compounds, doses and administration schemes are shown in Supplementary Table 9. Briefly, in the acute toxicity study, rats were administrated with the compounds at the indicated doses by oral gavage or via tail veins. The rats were clinically observed for 7–14 d after administration. In the repeated-dose toxicity study, rats were administered with compounds by gavage or via tail veins twice daily for 1 week. All animals were monitored for body weight, food intake and behaviours at least twice daily during the administration to detect signs of toxicity.

At the end of the experiment, samples of heart, liver, spleen, lung and kidneys were collected and processed for H&E staining for histological analysis.

Evaluation of in vitro antiviral activity. Calu3 and/or VeroE6-TMPRSS2 cells were infected with wild-type SARS-CoV-2 or variants (B.1.1.7, B.1.617.1, P.3 or B.1.1.529) at 0.01 multiplicity of infection (MOI) and 1 MOI, respectively, and treated with either Y180 or PF-07321332 in 5-fold serial dilution ranging from 0.0013 µM to 20 µM, or with vehicle or remdesivir (0.8, 4 or 20 µM). Cell lysates were collected at 24 h.p.i with RLT buffer for quantitative PCR with reverse transcription (RT–qPCR) analysis. The primer and probe sequences are provided in Supplementary Table 11.

Cell viability assay. VeroE6-TMPRSS2 cells were infected with wild-type SARS-CoV-2 or variants (B.1.1.7, B.1.617.1, P.3) at 1 MOI and treated with either Y180 in 5-fold serial dilution ranging from 0.0013 μM to 20 μM, or with vehicle or remdesivir (0.8, 4 or 20 μM). Cell viability was quantified by CellTiter-Glo luminescent cell viability assay kit (G7572, Promega) following the manufacturer's instructions, with a multilabel plate reader Victor X3 (Perkin Elmer) at 48 h.p.i[41].

Plaque reduction assay. VeroE6-TMPRSS2 cells were infected by wild-type SARS-CoV-2 or variants (B.1.1.7, B.1.617.1, P.3) with 50–70 plaque forming units (PFU) per well in a 12-well format. After inoculation, the cells were washed with PBS and covered with 2% agarose/PBS mixed with 2× DMEM/2% FBS at a 1:1 ratio, in the presence of either Y180 (5-fold dilution ranging from 0.0013 μM to 20 μM) or with vehicle only. Cells were fixed at 2 d.p.i. Fixed samples were stained with 0.5% crystal violet in 25% ethanol/distilled water for 10 min for plaque visualization.

SARS-CoV-2 infection in K18-hACE2 mice. K18-hACE2 transgenic mice aged 6–8 weeks were obtained from the Jackson Laboratory. The use of K18-hACE2 transgenic mice has received ethical approval from the Committee on the Use of Live Animals in Teaching and Research of The University of Hong Kong under Animal Ethics Committee at the University of Hong Kong (5779-21). On the day of infection, the hACE2 mice were intranasally inoculated with either 250 PFU B.1.1.7, 1×10^5 PFU B.1.617.1 or 2,000 PFU B.1.1.529, pre-diluted in 20 μl MEM. Mice were orally administered with 150 mg kg^{-1} dose^{-1} Y180 diluted in 180 μl 3% F188/45% PEG300/normal saline (for the treatment group) or PF-07321332 diluted in 180 μl 0.5% methylcellulose/2% Tween-80 or vehicle solution only (for the control group) twice daily for 8 d, or until sample collection or animal death. For the prophylactic treatment group, Y180 was administered at 1 h before virus challenge. For the therapeutic treatment group, Y180 administration was delayed until 6 h.p.i., while Y180 and ritonavir (10 mg kg^{-1} dose^{-1}, twice daily) or PF and ritonavir (10 mg kg^{-1} dose^{-1}, twice daily) administration was delayed until 16 h.p.i. Survival of the mice was monitored on a daily basis. Mice were killed at the designated timepoints and organ tissues were sampled for virological and histopathological analyses[29].

RNA extraction and RT-qPCR. Cell lysates and tissue samples were lysed using RLT buffer (Qiagen) and extracted with the RNeasy mini kit (74106, Qiagen). After RNA extraction, RT–qPCR was performed using the Transcriptor First Strand cDNA synthesis kit (04897030001, Roche), QuantiNova SYBR Green RT–PCR kit (208154, Qiagen) or the QuantiNova Probe RT–PCR kit (208354, Qiagen) with the LightCycler 480 real-time PCR System (Roche)[42]. The primer and probe sequences are provided in Supplementary Table 11.

Plaque assays. VeroE6-TMPRSS2 cells were seeded in 12-well plates 1 d before infection. The collected supernatant samples were serially diluted and inoculated to the cells for 1 h at 37 °C. After inoculation, the cells were washed with PBS 3 times and covered with 2% agarose/PBS mixed with 2× DMEM/2% FBS at a 1:1 ratio. The cells were fixed after incubation at 37 °C for 48 h. Fixed samples were stained with 0.5% crystal violet in 25% ethanol/distilled water for 10 min for plaque visualization[43].

Histology and immunohistochemistry staining. Histology and immunohistochemistry staining were performed using established protocols[44]. In brief, formic acid-soaked mice nasal turbinate and lung tissues were fixed overnight in 10% formalin. The fixed samples were then embedded in paraffin with a TP1020 Leica semi-enclosed benchtop tissue processor and sectioned at 5 μm. Tissue sections were fished and dried to fix on Superfrost Plus slides (Thermo Fisher) at 37 °C overnight. Afterwards, the sections were dewaxed and dehydrated in serially diluted xylene, ethanol and double-distilled water in sequence, co-heating together with antigen unmasking solution (H-3300, Vector Laboratories) at 85 °C for 90 s for antigen exposure, followed by blocking with 0.3% hydrogen peroxide for 30 min, and 1% BSA for 30 min. The in-house rabbit anti-SARS-CoV-2-N immune serum (1:5,000) and goat anti-rabbit IgG antibody (BA-1000-1.5, Vector Laboratories) (1:1,000) were applied as primary and secondary antibodies, respectively. The signal was developed with the 3,3'-diaminobenzidine (DAB) substrate kit (SK-4100, Vector Laboratories). Cell nuclei were labelled with Gill's haematoxylin. The slides were mounted with antifade mounting medium with DAPI (H-1200, Vector Laboratories). For H&E staining, infected tissue sections were stained with Gill's hematoxylin and eosin Y (Thermo Fisher). Images were taken with the Olympus BX53 light microscope (Olympus Life Science). The histology findings made in our current study represent unbiased description for the pathological damage in the tissues examined and the results were validated by an experienced pathologist in a blinded manner.

Statistical analysis. Data on figures represent mean ± s.d. All data were analysed with GraphPad Prism 7.0 and 8.0 software. Statistical comparison between different groups was performed by one-way analysis of variance (ANOVA) or log-rank (Mantel-Cox) test. All *t*-test performed in this study is two-tailed. Differences were considered statistically significant when $P<0.05$ ($^*P<0.05$, $^{**}P<0.01$, $^{***}P<0.001$, $^{****}P<0.0001$).

Reporting Summary. Further information on research design is available in the Nature Research Reporting Summary linked to this article.

Data availability

The coordinates and structure factors of SARS-CoV-2 M^{pro} in complex with (*R*)-**1a**, Y180 have been deposited into PDB with accession numbers 7FAY and 7FAZ, respectively. The complete sequence of SARS-CoV-2 HKU-001a (GenBank: MT230904), B.1.1.7/Alpha (GenBank: OM212469), B.1.617.1/Kappa (GISAID: EPI_ISL_2423557), P.3/Theta (GISAID: EPI_ISL_1660475) and B.1.529/Omicron (GenBank accession number OM212472) are available on GenBank. Additional data are provided in Supplementary information. Source data are provided with this paper.

Received: 20 January 2022; Accepted: 4 April 2022;
Published online: 27 April 2022

References

1. Harvey, W. T. et al. SARS-CoV-2 variants, spike mutations and immune escape. *Nat. Rev. Microbiol.* **19**, 409–424 (2021).
2. Shuai, H. et al. Attenuated replication and pathogenicity of SARS-CoV-2 B.1.1.529 Omicron. *Nature* **603**, 693–699 (2022).
3. Liu, L. et al. Striking antibody evasion manifested by the Omicron variant of SARS-CoV-2. *Nature* **602**, 676–681 (2021).
4. Kissler, S. M., Tedijanto, C., Goldstein, E., Grad, Y. H. & Lipsitch, M. Projecting the transmission dynamics of SARS-CoV-2 through the postpandemic period. *Science* **368**, 860–868 (2020).
5. Telenti, A. et al. After the pandemic: perspectives on the future trajectory of COVID-19. *Nature* **596**, 495–504 (2021).
6. Anand, K., Ziebuhr, J., Wadhwani, P., Mesters, J. R. & Hilgenfeld, R. Coronavirus main proteinase (3CL^{pro}) structure: basis for design of anti-SARS drugs. *Science* **300**, 1763–1767 (2003).
7. Hilgenfeld, R. From SARS to MERS: crystallographic studies on coronaviral proteases enable antiviral drug design. *FEBS J.* **281**, 4085–4096 (2014).
8. Lu, L., Su, S., Yang, H. & Jiang, S. Antivirals with common targets against highly pathogenic viruses. *Cell* **184**, 1604–1620 (2021).
9. Jin, Z. et al. Structure of M^{pro} from SARS-CoV-2 and discovery of its inhibitors. *Nature* **582**, 289–293 (2020).
10. Zhang, L. et al. Crystal structure of SARS-CoV-2 main protease provides a basis for design of improved α-ketoamide inhibitors. *Science* **368**, 409–412 (2020).
11. Dai, W. et al. Structure-based design of antiviral drug candidates targeting the SARS-CoV-2 main protease. *Science* **368**, 1331–1335 (2020).
12. Boras, B. et al. Preclinical characterization of an intravenous coronavirus 3CL protease inhibitor for the potential treatment of COVID19. *Nat. Commun.* **12**, 6055 (2021).
13. Qiao, J. et al. SARS-CoV-2 M^{pro} inhibitors with antiviral activity in a transgenic mouse model. *Science* **371**, 1374–1378 (2021).
14. Ma, C. et al. Boceprevir, GC-376, and calpain inhibitors II, XII inhibit SARS-CoV-2 viral replication by targeting the viral main protease. *Cell Res.* **30**, 678–692 (2020).
15. Kitamura, N. et al. Expedited approach toward the rational design of noncovalent SARS-CoV-2 main protease inhibitors. *J. Med. Chem.* **64**, 2848–2865 (2022).
16. Zaidman, D. et al. An automatic pipeline for the design of irreversible derivatives identifies a potent SARS-CoV-2 M^{pro} inhibitor. *Cell Chem. Biol.* **8**, 1–12 (2021).
17. Owen, D. R. et al. An oral SARS-CoV-2 M^{pro} inhibitor clinical candidate for the treatment of COVID-19. *Science* **374**, 1586–1593 (2021).
18. Ma, C. et al. Discovery of di- and trihaloacetamides as covalent SARS-CoV-2 main protease inhibitors with high target specificity. *J. Am. Chem. Soc.* **143**, 20697–20709 (2021).
19. Unoh, Y. et al. Discovery of S-217622, a non-covalent oral SARS-CoV-2 3CL protease inhibitor clinical candidate for treating COVID-19. *J. Med. Chem.* https://doi.org/10.1021/acs.jmedchem.2c00117 (2022).
20. Zhu, W. et al. Identification of SARS-CoV-2 3CL protease inhibitors by a quantitative high-throughput screening. *ACS Pharmacol. Transl. Sci.* **3**, 1008–1016 (2020).
21. Drayman, N. et al. Masitinib is a broad coronavirus 3CL inhibitor that blocks replication of SARS-CoV-2. *Science* **373**, 931–936 (2021).
22. Ugi, I., Meyr, R., Fetzer, U. & Steinbrückner, C. Versuche mit Isonitrilen. *Angew. Chem.* **71**, 386 (1959).
23. Dömling, A. & Ugi, I. Multicomponent reactions with isocyanides. *Angew. Chem. Int. Ed.* **39**, 3168–3210 (2000).
24. Jacobs, J. et al. Discovery, synthesis, and structure-based optimization of a series of *N*-(tert-butyl)-2-(*N*-arylamido)-2-(pyridin-3-yl) acetamides (ML188) as potent noncovalent small molecule inhibitors of the severe acute respiratory syndrome coronavirus (SARS-CoV) 3CL protease. *J. Med. Chem.* **56**, 534–546 (2013).

25. Bauer, R. A. Covalent inhibitors in drug discovery: from accidental discoveries to avoided liabilities and designed therapies. *Drug Discov. Today* **20**, 1061–1073 (2015).
26. Knoche, B. & Blaschke, G. Investigations on the in vitro racemization of thalidomide by high-performance liquid chromatography. *J. Chromatogr. A* **666**, 235–240 (1994).
27. DeWitt, S., Czarnik, A. W. & Jacques, V. Deuterium-enabled chiral switching (DECS) yields chirally pure drugs from chemically interconverting racemates. *ACS Med. Chem. Lett.* **11**, 1789–1792 (2020).
28. Pirali, T., Serafini, M., Cargnin, S. & Genazzani, A. A. Applications of deuterium in medicinal chemistry. *J. Med. Chem.* **62**, 5276–5297 (2019).
29. Shuai, H. et al. Emerging SARS-CoV-2 variants expand species tropism to murines. *eBioMedicine* **73**, 103643 (2021).
30. Zheng, J. et al. COVID-19 treatments and pathogenesis including anosmia in K18-hACE2 mice. *Nature* **589**, 603–607 (2021).
31. Winkler, E. S. et al. SARS-CoV-2 infection of human ACE2-transgenic mice causes severe lung inflammation and impaired function. *Nat. Immunol.* **21**, 1327–1335 (2020).
32. Oladunni, F. S. et al. Lethality of SARS-CoV-2 infection in K18 human angiotensin-converting enzyme 2 transgenic mice. *Nat. Commun.* **11**, 6122 (2020).
33. Chu, H. et al. Comparative tropism, replication kinetics, and cell damage profiling of SARS-CoV-2 and SARS-CoV with implications for clinical manifestations, transmissibility, and laboratory studies of COVID-19: an observational study. *Lancet Microbe* **1**, e14–e23 (2020).
34. Kabsch, W. XDS. *Acta Crystallogr. D* **66**, 125–132 (2010).
35. Evans, P. R. & Murshudov, G. N. How good are my data and what is the resolution? *Acta Crystallogr. D* **69**, 1204–1214 (2013).
36. McCoy, A. J. et al. Phaser crystallographic software. *J. Appl. Crystallogr.* **40**, 658–674 (2007).
37. Emsley, P., Lohkamp, B., Scott, W. G. & Cowtan, K. Features and development of Coot. *Acta Crystallogr. D* **66**, 486–501 (2010).
38. Bricogne, G. et al. BUSTER version 2.10.3 (Global Phasing, 2017).
39. Afonine, P. V. et al. Towards automated crystallographic structure refinement with phenix.refine. *Acta Crystallogr. D* **68**, 352–367 (2012).
40. Bredenbach, J. et al. Targeting the main protease of SARS-CoV-2: from the establishment of high throughput screening to the design of tailored inhibitors. *Angew. Chem. Int. Ed.* **60**, 10423–10429 (2021).
41. Chu, H. et al. Targeting highly pathogenic coronavirus-induced apoptosis reduces viral pathogenesis and disease severity. *Sci. Adv.* **7**, eabf8577 (2021).
42. Chu, H. et al. Host and viral determinants for efficient SARS-CoV-2 infection of the human lung. *Nat. Commun.* **12**, 134 (2021).
43. Shuai, H. et al. Differential immune activation profile of SARS-CoV-2 and SARS-CoV infection in human lung and intestinal cells: implications for treatment with IFN-β and IFN inducer. *J. Infect.* **81**, e1–e10 (2020).
44. Chu, H. et al. SARS-CoV-2 induces a more robust innate immune response and replicates less efficiently than SARS-CoV in the human intestines: an ex vivo study with implications on pathogenesis of COVID-19. *Cell. Mol. Gastroenterol. Hepatol.* **11**, 771–781 (2021).

Acknowledgements

This work was supported by the National Natural Science Foundation of China (82130104 and 81930125 to S.Y.; 00402354A1028 to J.L.); 1.3.5 project for disciplines of excellence, West China Hospital, Sichuan University (ZYGD18001 and ZYXY21001 to S.Y.; ZYYC21008 to J.L.); the fast-track research fund on COVID-19 of Sichuan Province (2020YFS0006 to S.Y.) and the fast-track grants of SARS-CoV-2 research from West China Hospital, Sichuan University (HX-2019-nCoV-053 to S.Y.); the National Clinical Research Center for Geriatrics, West China Hospital, Sichuan University (Z2021JC008 to J.L.); National Key R&D Program of China (2021YFF0702004 to J.L.); National Natural Science Foundation of China Excellent Young Scientists Fund (Hong Kong and Macau) (32122001 to H.C.); the Health and Medical Research Fund (COVID190121, CID-HKU1-5, COVID1903010-14 and 20190652 to H.C. and J.F.-W.C.); the Food and Health Bureau, The Government of the Hong Kong Special Administrative Region; the General Research Fund (17118621 to H.C.) of Research Grants Council, The Government of the Hong Kong Special Administrative Region; Health@InnoHK, Innovation and Technology Commission, The Government of the Hong Kong Special Administrative Region; the Consultancy Service for Enhancing Laboratory Surveillance of Emerging Infectious Diseases and Research Capability on Antimicrobial Resistance for Department of Health of the Hong Kong Special Administrative Region Government; the National Program on Key Research Project of China (grant no. 2020YFA0707500 and 2020YFA0707504 to H.C. and J.F.-W.C.); Sanming Project of Medicine in Shenzhen, China (SZSM201911014 to J.F.-W.C. and K.-Y.Y.); the High-Level Hospital Program, Health Commission of Guangdong Province, China to J.F.-W.C. and K.-Y.Y.; the research project of Hainan academician innovation platform (YSPTZX202004 to J.F.-W.C. and K.-Y.Y.); the Hainan talent development project (SRC200003 to J.F.-W.C. and K.-Y.Y.); donations from the Lee Wan Keung Charity Foundation Limited, Richard Yu and Carol Yu, Shaw Foundation Hong Kong, Michael Seak-Kan Tong, May Tam Mak Mei Yin, the Hong Kong Sanatorium & Hospital, Marina Man-Wai Lee, and the Lo Ying Shek Chi Wai Foundation. We also thank the staff of the Shanghai Synchrotron Radiation Facility (SSRF) beamlines (Shanghai, China) for great support.

Author contributions

S.Y., H.C., J.L. and J.F.-W.C. conceived and supervised the research, and designed the experiments; S.Y., B.-X.Q., A.-J.X. and J.L. performed the drug design; S.Y., B.-X.Q., A.-J.X., X.-L.L., F.-L.W., M.-X.C., S.-Y.Z. and C.H. performed the chemical experiments and collected the data; R.Z. and J.-X.Q., with the assistance of K.W. and R.-J.Z., performed gene expression and protein purification, crystallization and diffraction data collection; R.Z. and J.L. determined and analysed the crystal structures; J.-X.Q. and W.-P.L. performed enzymatic inhibition assays, high-throughput drug screening and IC_{50} measurements; R.Z. and J.-X.Q. performed enzymatic activity assays, DSF assays and cellular cytotoxicity assay; H.S., Y.H., T.T.-T.Y. and C.Y. performed antiviral cellular assays and in vivo antiviral studies; G.-F.L., J.-X.Q., W.Y. and C.T. performed in vivo toxicity studies; S.Y., H.C., J.L., J.F.-W.C., K.-Y.Y., H.S., Y.H., J.-X.Q., Y.-Q.W., W.-M.L., R.Z., Y.-F.W. and M.W. analysed and discussed the data. S.Y., H.C., J.L. and J.F.-W.C., with the assistance of K.-Y.Y., B.-X.Q., H.S., A.-J.X., Y.H., R.Z. and J.-X.Q., wrote and revised the manuscript.

Competing interests

West China Hospital of Sichuan University has applied for a Chinese patent covering Y180 and related compounds in 2021 (application number: 202111494340.0). J.F.-W.C. has received travel grants from Pfizer Corporation Hong Kong and Astellas Pharma Hong Kong Corporation Limited and was an invited speaker for Gilead Sciences Hong Kong Limited and Luminex Corporation. The funding sources had no role in study design, data collection, analysis or interpretation, or the writing of the paper. The other authors declare no competing interests.

Additional information

Extended data is available for this paper at https://doi.org/10.1038/s41564-022-01119-7.

Supplementary information The online version contains supplementary material available at https://doi.org/10.1038/s41564-022-01119-7.

Correspondence and requests for materials should be addressed to Jasper Fuk-Woo Chan, Jian Lei, Hin Chu or Shengyong Yang.

Peer review information *Nature Microbiology* thanks Mark Broenstrup and the other, anonymous, reviewer(s) for their contribution to the peer review of this work. Peer reviewer reports are available.

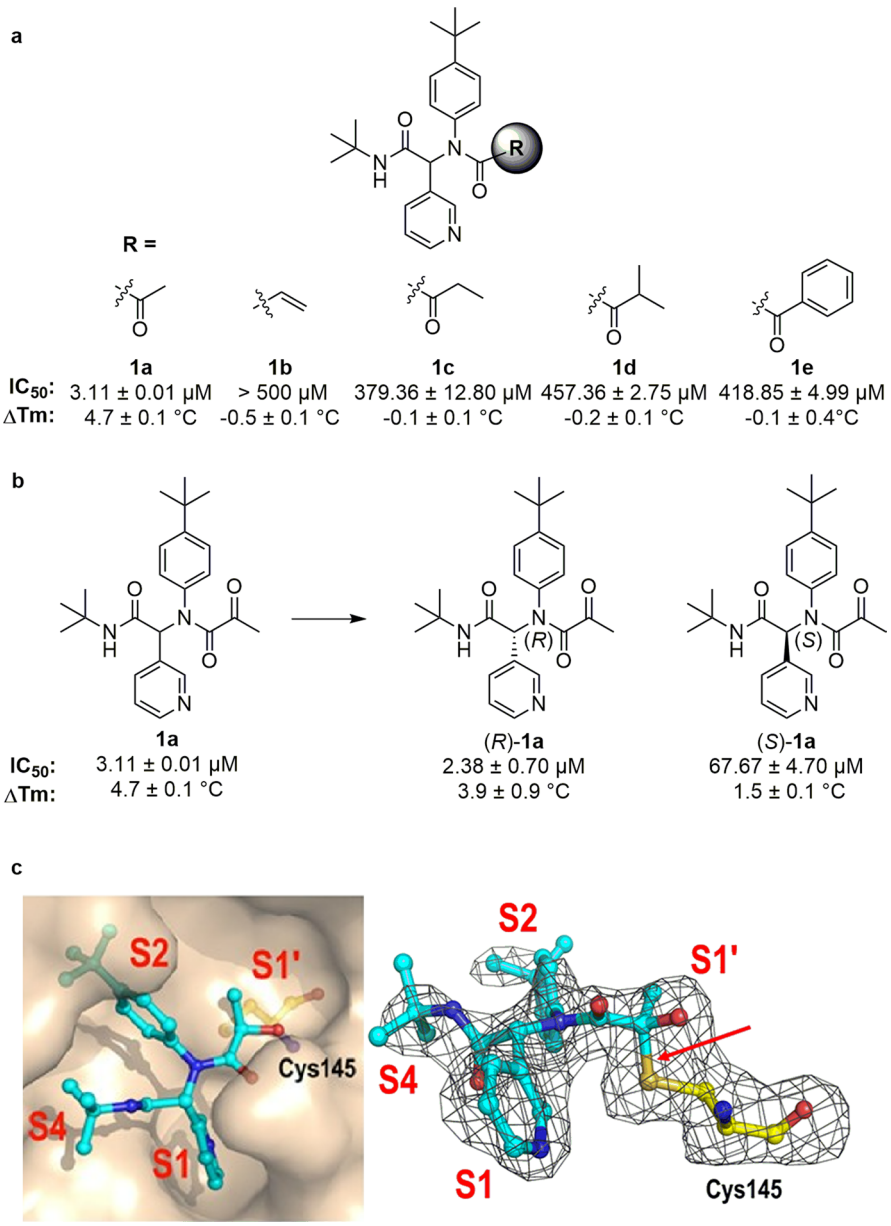

Extended Data Fig. 1 | Selection of a proper warhead at the R position. (a) Chemical structures and bioactivities of designed compounds **1a-e** (racemic mixture). Enzymatic inhibitory activities (IC_{50}) and biophysical activities (thermal shift (ΔTm) values) were measured by the FRET and DSF assays, respectively. Data are shown as mean ± SD, $n = 3$ biological replicates. **(b)** Racemic mixture **1a** was separated by chiral HPLC to stereoisomers (*R*)-**1a** and (*S*)-**1a**. **(c)** The active stereoisomer (*R*)-**1a** binding pocket of SARS-CoV M^{pro}. The molecule (*R*)-**1a** and Cys145 are displayed as sticks. The covalent bond (pointed by a red arrow) is formed between Cys145 and the warhead of (*R*)-**1a**. *Fo - Fc* density map (σ = 2.5) is shown in gray. Figure (c) was prepared using PyMOL (https://pymol.org).

a

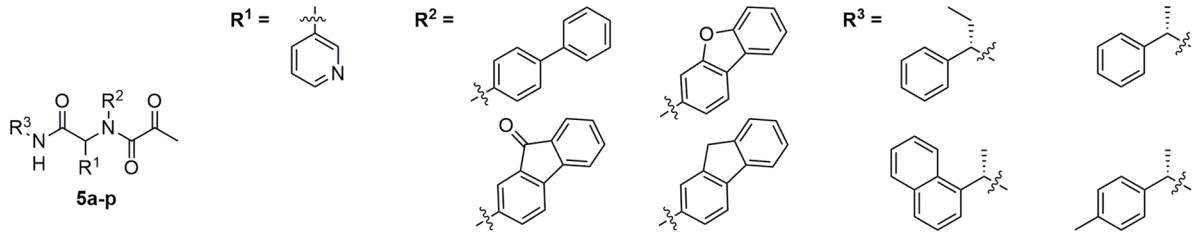

b

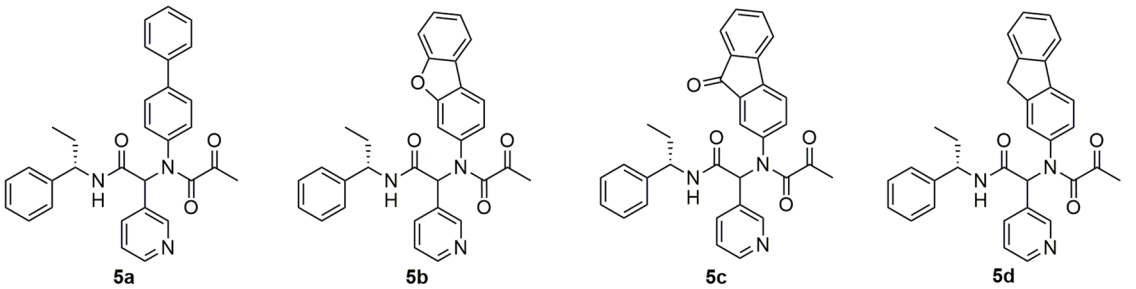

	5a	5b	5c	5d
Epimeric mixture:	40.8 ± 4.9 nM, 11.4 ± 1.7 °C	21.6 ± 0.6 nM, 14.7 ± 0.1 °C	35.4 ± 1.7 nM, 16.1 ± 0.1 °C	34.7 ± 1.1 nM, 14.9 ± 0.1 °C
(*R*)-epimer:	11.5 ± 0.3 nM, 26.0 ± 1.1 °C	11.3 ± 0.1 nM, 28.4 ± 0.1 °C	15.8 ± 0.6 nM, 17.6 ± 0.1 °C	14.8 ± 0.2 nM, 17.6 ± 0.1 °C
(*S*)-epimer:	1.90 ± 1.08 μM, 4.9 ± 0.2 °C	751.9 ± 1.4 nM, 8.9 ± 0.1 °C	430.1 ± 35.5 nM, 14.3 ± 0.9 °C	874.3 ± 10.6 nM, 8.6 ± 0.1 °C

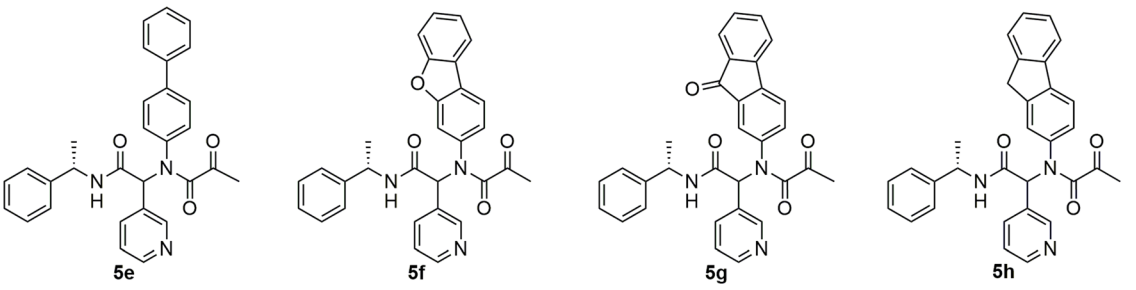

	5e	5f	5g	5h
Epimeric mixture:	60.8 ± 4.8 nM, 10.7 ± 3.1 °C	32.9 ± 4.8 nM, 11.7 ± 0.3 °C	45.9 ± 0.6 nM, 14.5 ± 0.5 °C	25.9 ± 0.6 nM, 11.6 ± 0.1 °C
(*R*)-epimer:	38.1 ± 2.6 nM, 12.9 ± 0.6 °C	13.8 ± 0.3 nM, 21.0 ± 0.1 °C	19.6 ± 0.3 nM, 17.4 ± 0.1 °C	14.8 ± 0.1 nM, 17.5 ± 0.1 °C
(*S*)-epimer:	2.80 ± 0.01 μM, 4.4 ± 0.1 °C	1.11 ± 0.03 μM, 9.2 ± 0.1 °C	1.60 ± 0.01 μM, 5.8 ± 0.2 °C	27.57 ± 1.62 μM, 1.7 ± 0.2 °C

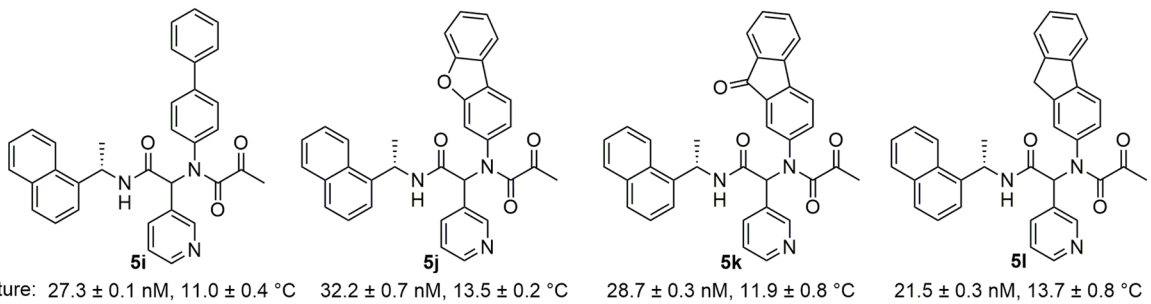

	5i	5j	5k	5l
Epimeric mixture:	27.3 ± 0.1 nM, 11.0 ± 0.4 °C	32.2 ± 0.7 nM, 13.5 ± 0.2 °C	28.7 ± 0.3 nM, 11.9 ± 0.8 °C	21.5 ± 0.3 nM, 13.7 ± 0.8 °C
(*R*)-epimer:	15.3 ± 0.3 nM, 16.2 ± 0.1 °C	13.3 ± 0.1 nM, 20.9 ± 3.8 °C	18.2 ± 0.7 nM, 13.1 ± 0.5 °C	14.0 ± 0.9 nM, 18.9 ± 0.1 °C
(*S*)-epimer:	1.42 ± 0.09 μM, 5.4 ± 0.9 °C	3.52 ± 0.03 μM, 3.9 ± 0.2 °C	5.71 ± 0.81 μM, 1.2 ± 0.1 °C	2.22 ± 0.01 μM, 4.7 ± 0.1 °C

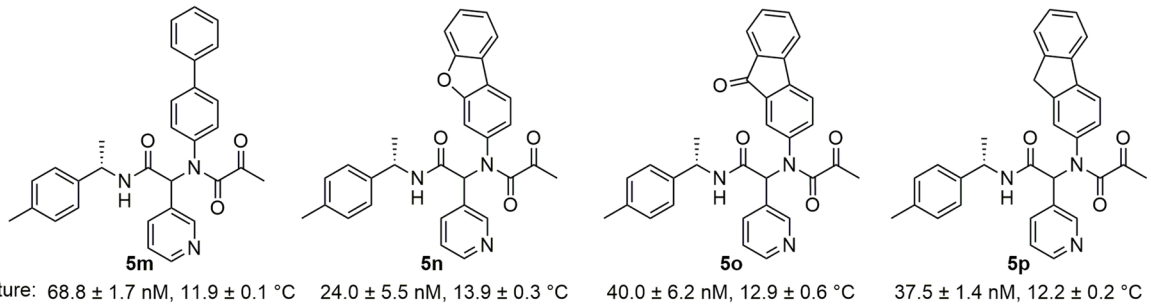

	5m	5n	5o	5p
Epimeric mixture:	68.8 ± 1.7 nM, 11.9 ± 0.1 °C	24.0 ± 5.5 nM, 13.9 ± 0.3 °C	40.0 ± 6.2 nM, 12.9 ± 0.6 °C	37.5 ± 1.4 nM, 12.2 ± 0.2 °C
(*R*)-epimer:	22.8 ± 3.4 nM, 15.0 ± 0.1 °C	15.2 ± 2.0 nM, 16.3 ± 0.3 °C	27.6 ± 0.8 nM, 16.2 ± 0.1 °C	25.1 ± 0.3 nM, 13.6 ± 0.1 °C
(*S*)-epimer:	3.21 ± 0.21 μM, 7.8 ± 0.1 °C	5.27 ± 0.60 μM, 7.6 ± 0.1 °C	1.19 ± 0.22 μM, 6.5 ± 0.4 °C	3.53 ± 0.55 μM, 7.7 ± 1.1 °C

Extended Data Fig. 2 | See next page for caption.

Extended Data Fig. 2 | Optimal fragments of R^1, R^2 and R^3, and chemical structures and bioactivities of compounds generated by combination of the optimal fragments. (a) Optimal fragments of R^1, R^2 and R^3 obtained in a stepwise optimization process. **(b)** Compounds **5a-p** [epimeric mixtures, *(R)*-epimers, and *(S)*-epimers]. Enzymatic inhibitory activities (IC_{50}) and biophysical activities [thermal shift (ΔTm) values] were measured by the FRET and DSF assays, respectively. Data are shown as mean $\pm$ SD, $n = 3$ biological replicates.

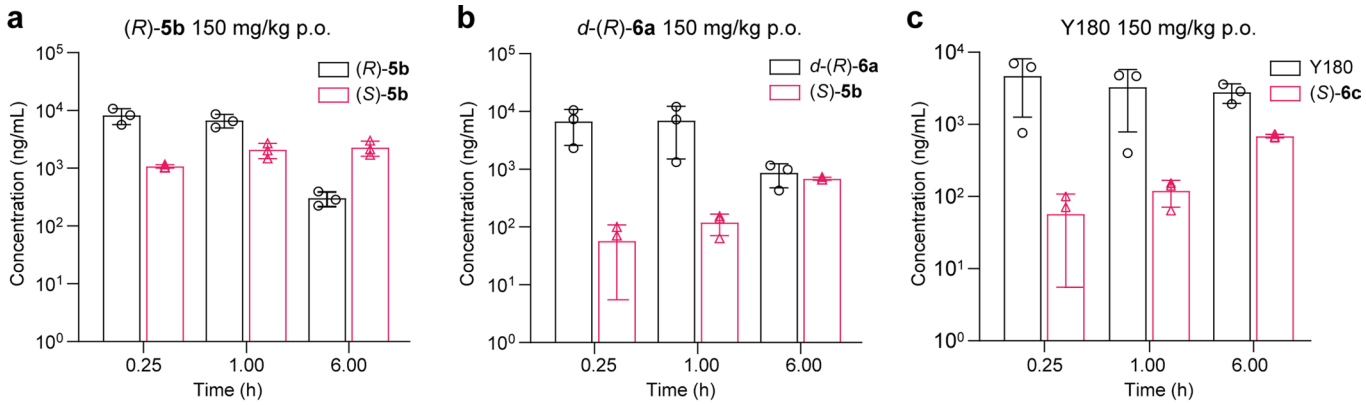

(*R*)-**5b** 150 mg/kg p.o.		
Time (h)	(*R*)-**5b**	(*S*)-**5b**
0.25	87.9	12.1
1	76.6	23.4
6	12.0	88.0

d-(*R*)-**6a** 150 mg/kg p.o.		
Time (h)	*d*-(*R*)-**6a**	(*S*)-**5b**
0.25	99.4	0.6
1	97.4	2.6
6	53.4	46.6

Y180 150 mg/kg p.o.		
Time (h)	Y180	(*S*)-**6c**
0.25	100.0	0.0
1	99.2	0.8
6	71.1	28.9

Extended Data Fig. 3 | Epimerization *in vivo* of (*R*)-5b, *d*-(*R*)-6a and Y180 in rats. (a-c) Plasma concentrations and ratios of (*R*)-**5b**, *d*-(*R*)-**6a** and Y180, and their corresponding epimers (*S*)-**5b**, (*S*)-**5b** and (*S*)-**6c** (with deuterium replaced by hydrogen; see Supplementary Fig. 9). All compounds were orally administrated in rats. Data are shown as mean ± SD, $n = 3$ biological replicates.

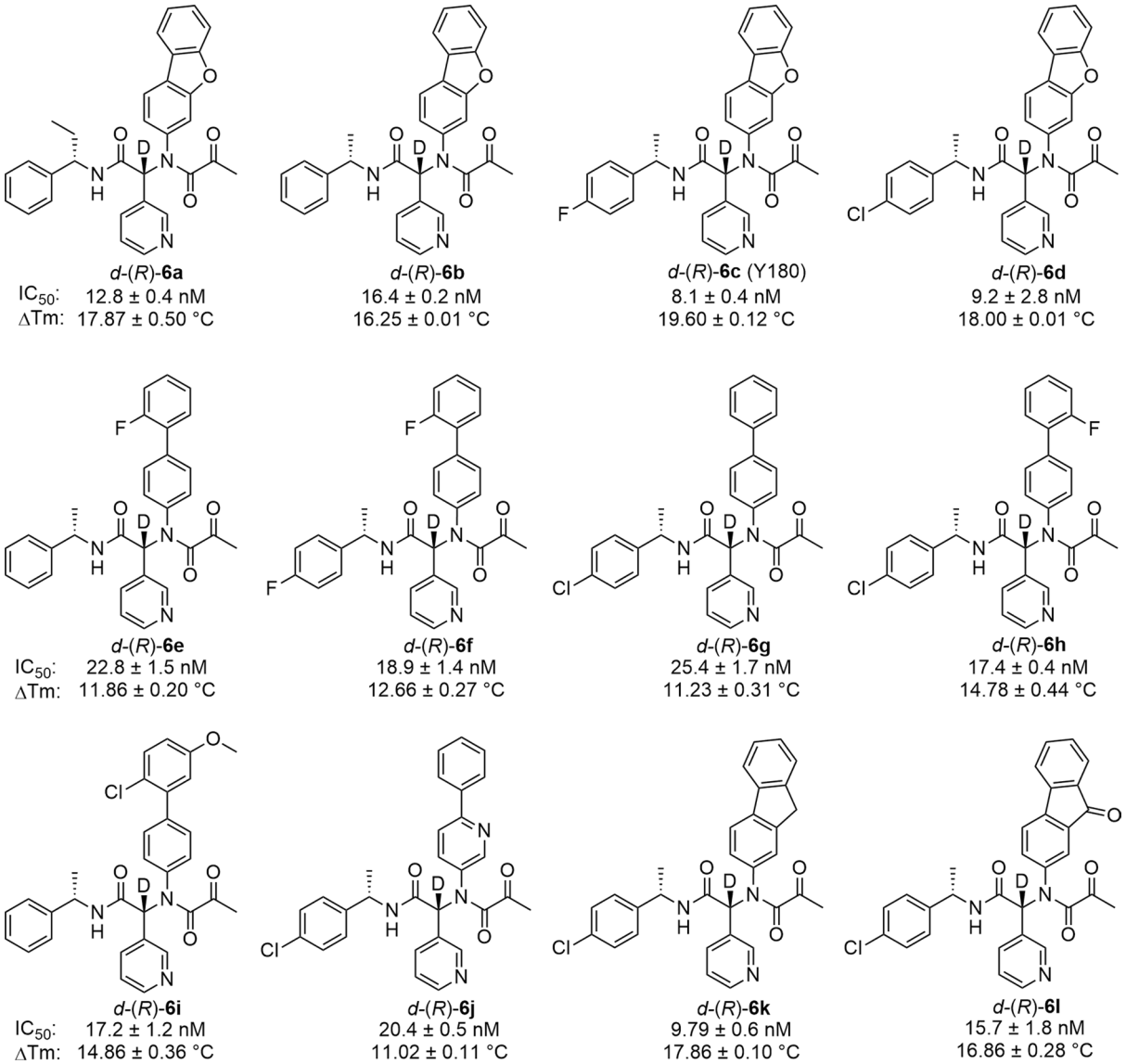

Extended Data Fig. 4 | Chemical structures and bioactivities of compounds *d*-(*R*)-6a-6l (*R*-epimers). Enzymatic inhibitory activities (IC_{50}) and biophysical activities (thermal shift ΔT_m) were measured by the FRET and DSF assays, respectively. Data are shown as mean ± SD, $n = 3$ biological replicates.

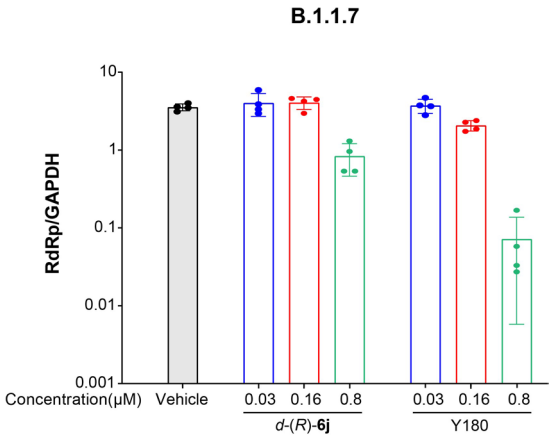

Extended Data Fig. 5 | Cellular antiviral activity of compounds Y180 [*d*-(*R*)-6c] and *d*-(*R*)-6j. VeroE6 cells were infected with SARS-CoV-2 B.1.1.7 strain at MOI of 0.01 and treated with different concentrations of tested compounds. At 24 h post infection, cell lysates were harvested for the detection of viral RNA-dependent RNA polymerase (RdRp) gene copies by RT-qPCR. Data are shown as mean ± SD, $n = 4$ biological replicates.

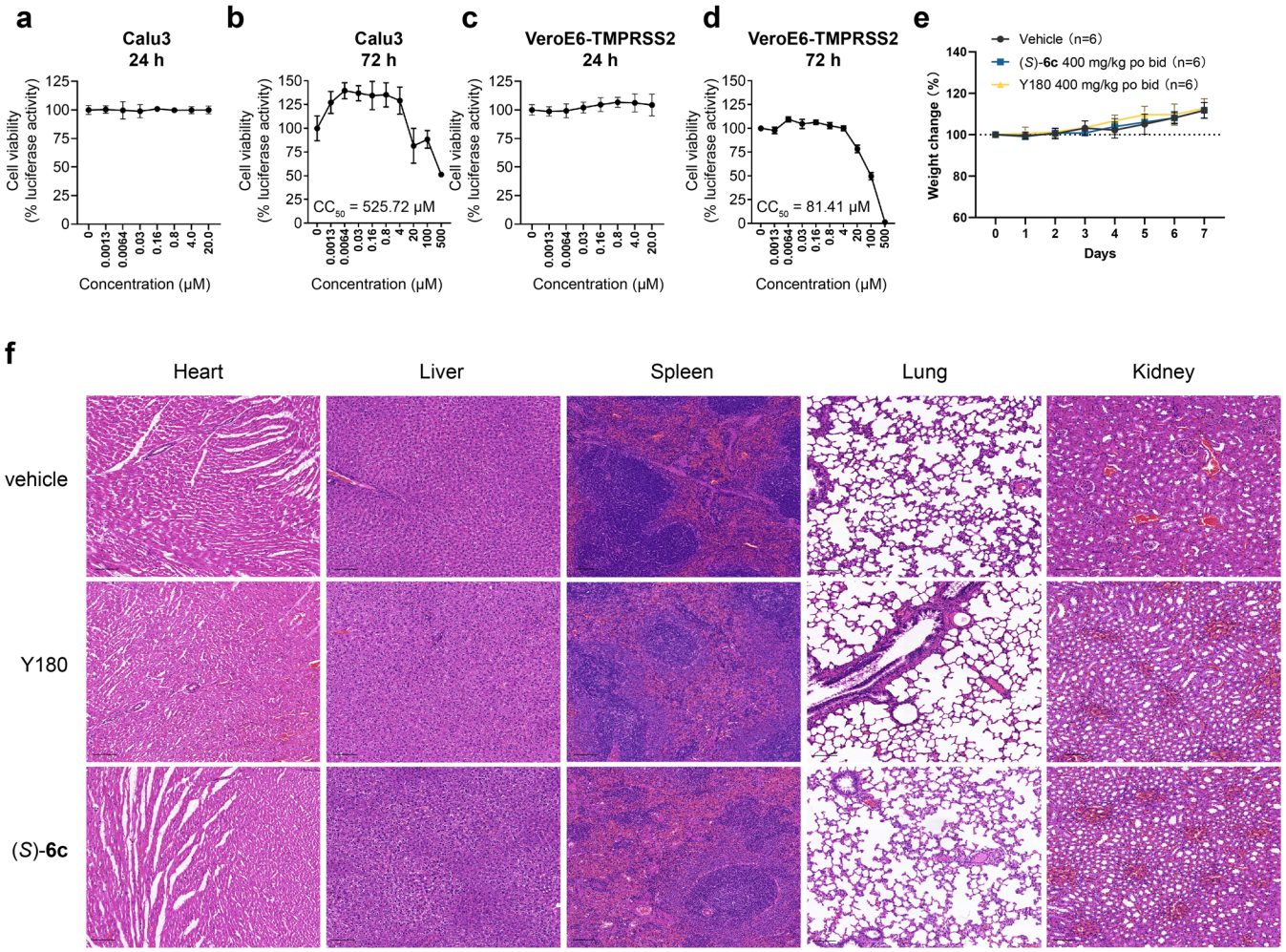

Extended Data Fig. 6 | *In vitro* cytotoxicity of Y180 and *in vivo* toxicity study of Y180 and (*S*)-6c. (a-d) Cells were treated with 5-fold serial diluted Y180 for 24 hours (**a** and **c**) or 72 hours (**b** and **d**) before cell viability was measured in (**a** and **b**) Calu3 and (**c** and **d**) Vero E6-TMPRSS2. Luciferase readings were normalized to mock treatment controls. Data are shown as mean ± SD, $n = 6$ biological replicates. **e**. Body weight change (percentage of initial body weight) with Y180 treatment (400 mg/kg/dose, twice per day) via oral delivery route for one week in rats ($n = 6$). **f**. Representative images of H&E staining of heart, liver, spleen, lung and kidney of rats orally treated with vehicle, Y180 and (*S*)-**6c**. Three randomly selected rats were sampled in each group were used for histology analysis. Scale bar represents 100 μm. CC_{50}, 50% cytotoxicity concentration.

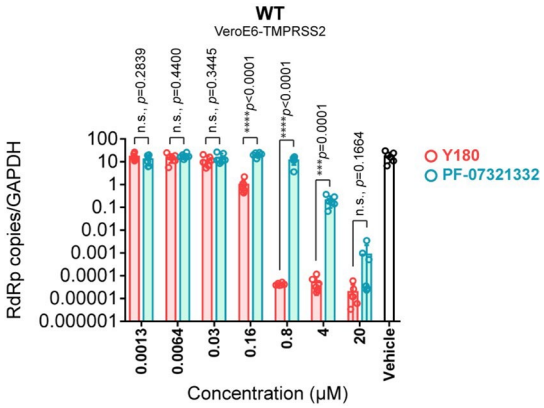

Extended Data Fig. 7 | Comparison of the *in vitro* antiviral efficacy between Y180 and PF-07321332. VeroE6-TMPRSS2 cells infected with wildtype SARS-CoV-2 at 0.01 MOI were treated with serially-diluted Y180 or PF-07321332. Lysates were harvested at 24 h.p.i. for the detection of polymerase (RdRp) gene copies with RT-qPCR ($n = 6$). All data are shown as mean ± SD. Data were obtained from three independent experiments. Statistical significance is assessed by Student's *t*-test. n.s., not statistically significant, *** represented $p < 0.001$; **** represented $p < 0.0001$.

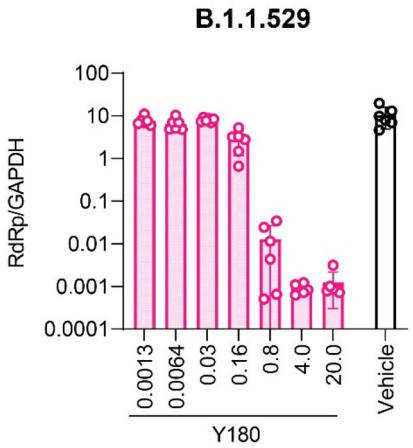

Extended Data Fig. 8 | *In vitro* effect of Y180 against the SARS-CoV-2 Omicron variant. VeroE6-TMPRSS2 cells were infected with SARS-CoV-2 Omicron variant at 0.01 MOI. Lysate were harvested at 24 h.p.i. for the detection of viral titer with RT-qPCR ($n = 6$). Viral RNA-dependent RNA polymerase (RdRp) gene copies in VeroE6-TMPRSS2 infected with B.1.1.529. Data are shown as mean ± SD. Data were obtained from three independent experiments.

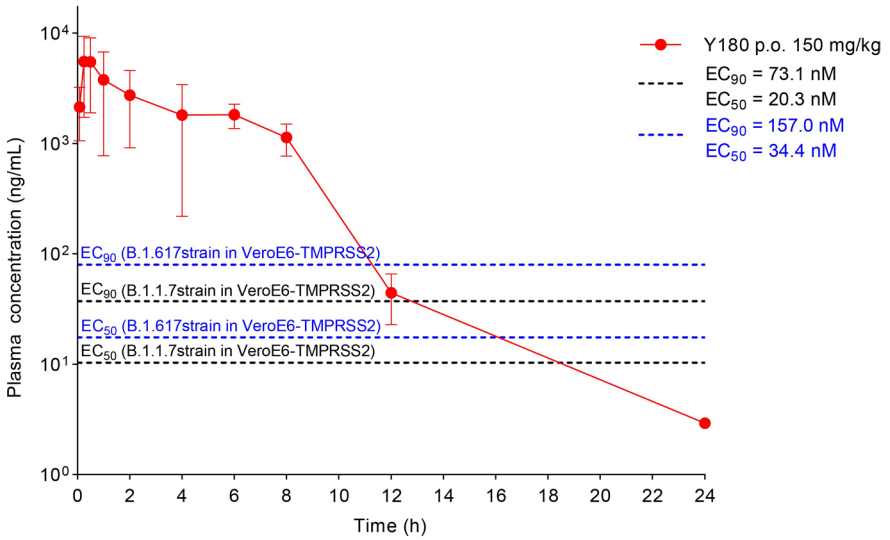

Extended Data Fig. 9 | Plasma concentration–time curves for Y180 in mice. The mean plasma concentration-time curves of Y180 (p.o. 150 mg/kg) in mice ($n = 3$). The EC_{50} and EC_{90} values of Y180 were calculated from the cell-based antiviral activity data obtained with VeroE6-TMPRSS2 cells infected with SARS-CoV-2 strain B.1.1.7 (black dashed lines) or B.1.617 (blue dashed lines). Data are shown as mean ± SD.

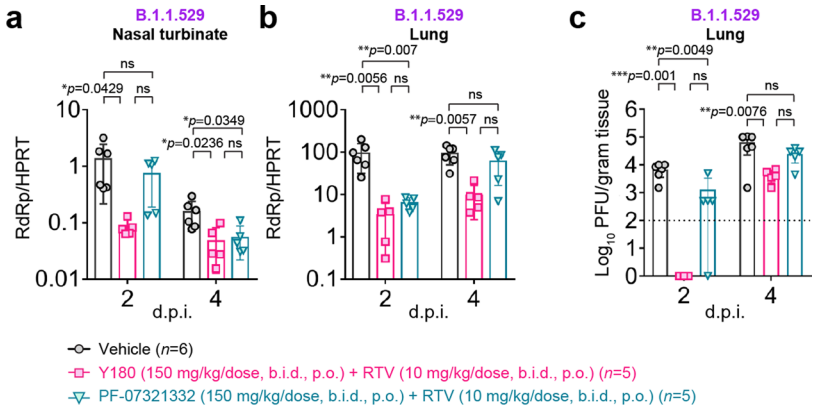

Extended Data Fig. 10 | Comparison of the *in vivo* antiviral therapeutic efficacy between Y180 and PF-07321332 in K18-hACE2 transgenic mice. K18-hACE2 transgenic mice were challenged with 2000 PFU B.1.1.529. Animals were orally administered with 150 mg/kg/dose Y180 with ritonavir (10 mg/kg/dose) or PF-07321332 with ritonavir (10 mg/kg/dose) or vehicle beginning 16 hours post-infection. ($n = 6$). Lung and nasal turbinate were collected on 2 and 4 d.p.i. for viral burden quantification with **(a-b)** RT-qPCR and **(c)** plaque assays. Statistical differences were determined with one-way analysis of variance (ANOVA) in **(a-c)**. n.s., not statistically significant, * represented $p < 0.05$; ** represented $p < 0.01$; *** represented $p < 0.001$. Data are shown as mean ± SD. Data were obtained from two independent experiments.

nature research

Corresponding author(s): Jasper Fuk-Woo Chan, Jian Lei, Hin Chu & Shengyong Yang

Last updated by author(s): Mar 30, 2022

Reporting Summary

Nature Research wishes to improve the reproducibility of the work that we publish. This form provides structure for consistency and transparency in reporting. For further information on Nature Research policies, see our Editorial Policies and the Editorial Policy Checklist.

Statistics

For all statistical analyses, confirm that the following items are present in the figure legend, table legend, main text, or Methods section.

n/a	Confirmed	
☐	☒	The exact sample size (*n*) for each experimental group/condition, given as a discrete number and unit of measurement
☐	☒	A statement on whether measurements were taken from distinct samples or whether the same sample was measured repeatedly
☐	☒	The statistical test(s) used AND whether they are one- or two-sided *Only common tests should be described solely by name; describe more complex techniques in the Methods section.*
☒	☐	A description of all covariates tested
☒	☐	A description of any assumptions or corrections, such as tests of normality and adjustment for multiple comparisons
☐	☒	A full description of the statistical parameters including central tendency (e.g. means) or other basic estimates (e.g. regression coefficient) AND variation (e.g. standard deviation) or associated estimates of uncertainty (e.g. confidence intervals)
☐	☒	For null hypothesis testing, the test statistic (e.g. *F*, *t*, *r*) with confidence intervals, effect sizes, degrees of freedom and *P* value noted *Give P values as exact values whenever suitable.*
☒	☐	For Bayesian analysis, information on the choice of priors and Markov chain Monte Carlo settings
☒	☐	For hierarchical and complex designs, identification of the appropriate level for tests and full reporting of outcomes
☒	☐	Estimates of effect sizes (e.g. Cohen's *d*, Pearson's *r*), indicating how they were calculated

Our web collection on statistics for biologists contains articles on many of the points above.

Software and code

Policy information about availability of computer code

Data collection	CLARIOstar (v5.61); Bio-Rad CFX Maestro 1.1 (v4.1.2433.1219); Agilent 1200 series HPLC (Agilent Technologies, Palo Alto, CA, USA); API4000 mass spectrometer (Applied Biosystems/MDS Sciex, Toronto, Canada); Victor X3 (Perkin- Elmer); LightCycler 480 Real-Time PCR System (Roche, Basel, Switzerland)
Data analysis	MestReNova (12.0.2); GraphPad Prism; Pymol (version 2.4.0); CCP4 (version 7.0.078); Coot (version 0.8.9.2); BUSTER (version 2.10.3); XDS (version 20200131); Phenix(Version 1.18.2_3874)

For manuscripts utilizing custom algorithms or software that are central to the research but not yet described in published literature, software must be made available to editors and reviewers. We strongly encourage code deposition in a community repository (e.g. GitHub). See the Nature Research guidelines for submitting code & software for further information.

Data

Policy information about availability of data

All manuscripts must include a data availability statement. This statement should provide the following information, where applicable:

- Accession codes, unique identifiers, or web links for publicly available datasets
- A list of figures that have associated raw data
- A description of any restrictions on data availability

SARS-CoV-2 HKU-001a (GenBank accession number MT230904), B.1.1.7 (GISAID: EPI_ISL_1273444), B.1.617.1 (GISAID: EPI_ISL_2423557), P.3 (GISAID: EPI_ISL_1660475), and B.1.529 (GISAID: EPI_ISL_OM212472) were isolated from laboratory-confirmed COVID-19 patients in Hong Kong. The complete sequence of SARS-CoV-2 HKU-001a (GenBank: MT230904), B.1.1.7/Alpha (GenBank: OM212469), B.1.617.1/Kappa (GISAID: EPI_ISL_2423557), P.3/ Theta (GISAID: EPI_ISL_1660475), and B.1.529/ Omicron (GenBank accession number OM212472) are available on GenBank.
The X-ray data sets generated during and/or analyzed during the current study are available in the PDB repository. RCSB website: http://www.rcsb.org/pdb.

Accession code for X-ray structure of (R)-1a is 7FAY. Accession code for X-ray structure of Y180 is 7FAZ.
All source data is provided in the source data.

Field-specific reporting

Please select the one below that is the best fit for your research. If you are not sure, read the appropriate sections before making your selection.

☒ Life sciences ☐ Behavioural & social sciences ☐ Ecological, evolutionary & environmental sciences

For a reference copy of the document with all sections, see nature.com/documents/nr-reporting-summary-flat.pdf

Life sciences study design

All studies must disclose on these points even when the disclosure is negative.

Sample size	Sample size estimation was not relevant for this study, as it does not report on a statistical evaluation of effects between two or more groups. For the animal study except in vivo antiviral study, the numbers of animals in each group meet the requirement for statistical analysis (at least 3 for each group), which is sufficient given the excellent technical reproducibility. For in vivo antiviral study, group sizes were chosen based on statistical power analysis and our prior experience in examining viral titers in SARS-CoV-2 infected K18-hACE2 transgenic. Experiments were repeated to give a sample size of 5 or above.
Data exclusions	No data has been excluded from the analyses presented in this manuscript.
Replication	To ensure reproducibility of experimental findings, each assay was performed at least two times to confirm the results. IC50 measurements were carried out with three biological replicates for each data point and these data were used to calculate mean values. DSF assays were carried out with three biological replicates for each data point and these data were used to calculate mean values. Cytotoxicity assays were carried out with three biological replicates. Antiviral activity assays (RT-qPCR and cell protection assay) were performed at least in three biological replicates. In animal studies, multiple mice were included in each group. In in vivo antiviral studies, all were performed in two separate occasions. Reproducible findings were obtained from all repeats.
Randomization	For all in vivo experiments, gender- and age- matched mice were randomized into different experimental groups. Mice were randomly assigned to groups for infection and treatment, and were then housed as a group in a cage for the duration of the experiment. For the in vitro experiments, cells were randomized into different infection/treatment groups. The tests were also randomly selected from all samples. The pictures were representatively shown.
Blinding	For the measurement of quantitative values, such as viral genome copies, infectious viral titers, cytokine/chemokine gene copies, body weight and survival, data acquiring does not involve subjective judgments, therefore no blinding procedures were applied to the experimentalists involved. For the in vitro and in vivo experiments, blinding was not possible because researchers were involved in infection/treatment procedures. For the histological examinations, qualified pathologists were blinded to group allocation to ensure the assessment was unbiased.

Reporting for specific materials, systems and methods

We require information from authors about some types of materials, experimental systems and methods used in many studies. Here, indicate whether each material, system or method listed is relevant to your study. If you are not sure if a list item applies to your research, read the appropriate section before selecting a response.

Materials & experimental systems

n/a	Involved in the study
☐	☒ Antibodies
☐	☒ Eukaryotic cell lines
☒	☐ Palaeontology and archaeology
☐	☒ Animals and other organisms
☒	☐ Human research participants
☒	☐ Clinical data
☒	☐ Dual use research of concern

Methods

n/a	Involved in the study
☒	☐ ChIP-seq
☒	☐ Flow cytometry
☒	☐ MRI-based neuroimaging

Antibodies

Antibodies used	In-house rabbit anti-SARS-CoV-2-N immune serum (1:5000) Goat anti-rabbit IgG antibody (BA-1000-1.5, Vector Laboratories) (1:1000)
Validation	Commercial primary antibodies were validated by the manufacturers.The in-house anti-SARS-CoV-2-N and anti-SARS-CoV-N immune serum were validated with ELISA, Western blots, and immunofluorescence staining.

Eukaryotic cell lines

Policy information about cell lines

Cell line source(s)	Huh7, BEAS-2B and HUVEC cells were purchased from Cell Bank of Chinese Academy of Sciences. A549, VERO E6, Calu3 cells were purchased from ATCC. VeroE6-TMPRSS2 cells were obtained from the Japanese Collection of Research Bioresources (JCRB 1819) Cell Bank.
Authentication	All the cell lines were commercially available and have not been authenticated after receiving them.
Mycoplasma contamination	Mycoplasma testing confirmed negative at regular intervals.
Commonly misidentified lines (See ICLAC register)	No commonly misidentified cell lines were used.

Animals and other organisms

Policy information about studies involving animals; ARRIVE guidelines recommended for reporting animal research

Laboratory animals	Male SD rats, male ICR (Institute of Cancer Research) mice or beagle dogs (n = 3 per group, aged 1~2 years and weighting 9~12 kg) were used to pharmacokinetic (PK) studies. SD (Sprague Dawley) rats (age: 7-11 weeks) consist of half male (weight: 200-230 g) and half female (weight: 190-220 g) were used to assess toxicity of Y180 and (S)-6c in vivo. Female or male K18-hACE2 transgenic mice (2B6. Cg-Tg(k18-ACE2)2Prlmn/J), aged from 6-8 weeks, were used to in vivo studies. The mice were kept in cages with individual ventilation under 65% humidity and an ambient temperature of 21–23 °C and a 12 h–12 h day–night cycle for housing and husbandry.
Wild animals	The study did not involve wild animals.
Field-collected samples	The study did not involve samples collected from the field.
Ethics oversight	The PK studies were approved by the ethics committee the Institute Animal Care and Use Committee (IACUC) of Shanghai Medicilon Inc., ZLA (Beijing) Pharmaceutical Technology Co. Ltd and Sichuan Greentech Biotechnology Co. Ltd. The in vivo toxicity study was approved by the Ethical and Animal Welfare Committees of West China Hospital, Sichuan University (20211063A). The use of K18-hACE2 transgenic mice was received ethical approval from the Committee on the Use of Live Animals in Teaching and Research of The University of Hong Kong under Animal Ethics Committee at the University of Hong Kong (5779-21).

Note that full information on the approval of the study protocol must also be provided in the manuscript.